## A Mean-Field Firing-Rate Model for the Suprachiasmatic Nucleus\*

Alexander G. Ginsberg<sup>†</sup> and Victoria Booth<sup>‡</sup>

Abstract. We present a mean-field formalism for modeling firing-rate statistics of brain regions whose neurons exhibit atypical firing patterns and heterogeneous electrophysiological properties. We apply the formalism to the suprachiasmatic nucleus (SCN)—the human circadian pacemaker—whose neurons can intrinsically exhibit depolarized low-amplitude membrane oscillations (DLAMOs), depolarization block (DB), and standard action potential firing at different times of day. Further, gammaaminobutyric acid reversal potentials and molecular circadian phases of SCN neurons, among other properties, vary across the network and/or slowly over time. Our formalism consists of a system of integro-differential equations describing the time evolution of the mean and standard deviation of synaptic conductances across the network. Electrophysiological properties of SCN neurons are incorporated by computing responses to synaptic conductance inputs of a Hodgkin–Huxley-type SCN neuron model that exhibits DLAMOs and DB. Such responses are then averaged over distributions of relevant quantities and included in the differential equations. Results suggest mechanisms by which physiologically relevant changes to firing activities may arise, highlighting means by which the amplitude of firing rates may shrink, the standard deviation of firing rates may grow, and by which a mid-day dip in firing rates may appear. For instance, results show that a large spread in circadian phases across SCN neurons reduces the size of oscillations in SCN network firing activity across the 24-hour day, identifying a mechanism by which heterogeneities in neuron electrophysiology could influence circadian rhythms.

**Key words.** population firing rates, neural mass models, SCN, circadian rhythms, ensemble statistics, integrodifferential equations

MSC codes. 45J05, 92B25, 92C20, 82D99

**DOI.** 10.1137/22M1496256

1. Introduction. Firing-rate, neural-mass, and mean-field models are successful mathematical reductions for the high-dimensional nonlinear systems representing neuronal networks and their activity. These models describe average neural firing activity levels across a network. Thus, they are particularly relevant for networks of neurons where the assumed pertinent information is carried in the neural firing rate, rather than in the timing of individual neuron spikes relative to each other. The suprachiasmatic nucleus (SCN) in the hypothalamus, the central circadian pacemaker in mammals, is an example of a rate-coding neural population. Indeed, its 24-hour variation in average neuron firing rates is assumed to be the primary driver

<sup>\*</sup>Received by the editors May 16, 2022; accepted for publication (in revised form) by K. Tsaneva-Atanasova August 17, 2022; published electronically February 3, 2023.

https://doi.org/10.1137/22M1496256

Funding: This work was supported by National Science Foundation grant DMS-1853506.

Department of Mathematics, University of Michigan, Ann Arbor, MI 48103 USA (ginsbera@umich.edu).

<sup>&</sup>lt;sup>‡</sup>Departments of Mathematics and Anesthesiology, University of Michigan, Ann Arbor, MI 48103 USA (vbooth@umich.edu).

for transmission of daily circadian timing information to downstream targets [26]. There is evidence for this transmission to occur via synaptic signaling and humoral signaling [32].

Perhaps the most well-known class of firing-rate models are "convolutional models," which assume that a network of neurons may be reduced to several interacting populations. The firing activity of each population is modeled as a deterministic, often sigmoidal, gain function of the population's inputs. The time evolution of such firing activity is then typically modeled using differential equations whose solutions are convolution integrals over time. The most well known among such models is the Wilson–Cowan neural mass [53]. It models a cortical brain area with interacting excitatory and inhibitory populations and outputs the proportion of neurons which are firing in each population over time. Next-generation firing-rate models seek to improve upon these models by replacing the logistic gain functions with more accurate functions of neural responses (such as frequency-current curves) [55] or of network population activity [10].

In classic firing-rate models, state variables represent averages of important quantities across the network, such as average membrane voltages and average firing rates. Thus, they do not account for variability of network properties, as may be caused by heterogeneity in neural responses, synaptic signals or connectivity, and can lead to variations in neural activity across the network. Population density approaches account for variability by starting with a simple model of a spiking neuron and deriving a Fokker–Plank equation for the time-evolution of a probability density function of membrane voltages (see, e.g., [15, 20]). However, obtaining expressions for such probability densities is often computationally intensive. Furthermore, obtaining resulting average firing rates can be complex, especially for more biophysically accurate neural responses. An alternate neural mass model formalism was proposed by Zandt et al. [55] that accounts for the time evolution of distributions of synaptic currents by assuming a normal distribution of currents and firing rates across the network. This results in integro-differential equations that model the time evolution of approximations of the mean and standard deviation of synaptic currents and firing rates across the network.

While such formalisms have expanded the accuracy and range of applications of firing-rate models, recent results have identified properties of SCN neurons and their network that are not easily accounted for by these models. For example, while SCN population firing rates display a ~24-hour cycle with higher rates during the day (light period) and lower rates during the night (dark period), recordings of individual SCN neurons have identified atypical firing patterns across the circadian cycle [5]. Specifically, one class of SCN neurons displays the familiar action potential firing at varying rates throughout most of the 24-hour day, but during mid-day hours they enter electrically excited states. These states include depolarization block (DB) or a state characterized by low-amplitude oscillatory fluctuations in membrane potential, referred to as depolarized low-amplitude membrane oscillations (DLAMOs) [4, 5, 29, 46]. In the DLAMO state, membrane voltages oscillate nearly sinusoidally with a minimum well above resting membrane potential and peak well below the maximum voltage in typical action potential firing.

Another property of SCN population activity that challenges firing-rate reductions is heterogeneity of neural responses across the network. A primary facet of such heterogeneity lies in the "molecular clocks" contained in SCN neurons. Namely, the daily variations in SCN neuron firing patterns are generated by the intracellular transcription-translation feedback

loops (TTFLs) of circadian clock genes and proteins. These molecular clocks modulate the responses of SCN neurons to synaptic signalling, so that for some clock states the neuron never fires and in others the neuron fires spontaneously or exhibits DLAMOs given strong synaptic signaling. Under normal conditions, when circadian rhythms are entrained to the 24-hour environmental light cycle, cellular TTFL circadian clocks are approximately synchronized. As a result, SCN neurons may be assumed to be exhibiting oscillating firing patterns synchronized to the circadian clocks. However, this synchronization can be degraded by disruptions in light schedules as occurs in shift work and jet lag [42]. Additionally, degradation of clock cell synchrony may occur during aging [43]. This desynchrony of intracellular clocks presumably results in a wide variation in neural firing patterns and responses, i.e., action potential spiking, DLAMOs, or DB, across the SCN network. Physiologically, the resulting variation of the firing activity in the SCN has important consequences as it has been correlated with reduced amplitude of circadian signaling [23].

A further facet of heterogeneity in the SCN network lies in the function of gamma-aminobutyric acid (GABA), the primary synaptic neurotransmitter in the SCN [40]. GABA plays a somewhat unusual role in the SCN [16], wherein GABA-elicited postsynaptic currents (PSCs) can be either excitatory or inhibitory. This variability in GABA-mediated PSCs is due to variations in intracellular chloride concentrations which alter the synaptic current reversal potential in post-synaptic cells [16]. As a result, neuronal responses to synaptic currents can vary across the network leading to more variation in neural firing activity.

Thus, the rate code of circadian signaling by the SCN network is influenced by multiple factors not typically accounted for in firing-rate models: atypical neuron firing states as well as variations in neuron firing states and synaptic currents across the network.

In this paper, we derive a firing-rate model framework for the average network synaptic and firing activity, and their standard deviations, of a network of SCN neurons that exhibit diverse firing patterns across the circadian cycle. A strength of our approach is that it accounts for atypical neuron firing patterns and incorporates distributions of neuron firing properties and PSCs. While we derive the model for an SCN network, the formalism can be applied generally to other neural populations with unique and variable neural firing properties.

The paper is organized as follows. We derive and describe our firing-rate model framework in the most general context in section 2. We apply our model to the SCN network in section 3 and show the results of the application to the SCN in section 4. Finally, we provide concluding remarks that contextualize our formalism within the firing-rate model literature and highlight predictions made by our model about the SCN in section 5.

2. Firing-rate model derivation and description. Our firing-rate model formalism consists of a system of integro-differential equations describing the time evolution of the means and standard deviations of the firing rates and synaptic conductances across a single population of neurons, similar to [55]. In the model, the synaptic conductance statistics are the "model variables," in the sense that integrating the differential equations explicitly yields the synaptic conductance statistics as a function of time. The firing-rate means and standard deviations, on the other hand, are computed implicitly during numerical integration of the model.

While the statistics of the firing rates and synaptic conductances are the main variables in the model, a variety of other parameters play an important role. Foremost are the parameters whose values vary across the network. One such varying parameter is the number of incoming synaptic connections to each neuron,  $N_{syn}$ . Other such parameters, which we collectively refer to with the parameter vector  $\vec{P}(t)$  of dimension m, may include synaptic reversal potentials, such as the varying GABA reversal potential in the SCN, or parameters that influence the firing states of neurons, such as the time-varying phases of molecular clocks in the SCN. Notably, our model allows for time dependence in the vector of parameters  $\vec{P}(t)$ , so long as  $\vec{P}(t)$  varies on a much slower time scale than the time scale of synaptic integration.

To explain the derivation of the model, we first describe the postsynaptic response of a single neuron to synaptic input from multiple presynaptic cells (Figure 1 and section 2.1). We then describe the calculation of means and standard deviations of the neural responses across the network (Figure 2 and section 2.2). But first, we briefly summarize the derivation.

Consider the response of a postsynaptic cell i, at time t, that receives synaptic input from cell j. As described in section 2.1, we compute the synaptic conductance  $g_{ji}(t)$  which depends on two factors. One is the firing rate of presynaptic cell j just prior to time t,  $f_{j}(s)$ , and the other factor is the synaptic response function  $H_{\alpha}$  which describes the time-varying postsynaptic response to a presynaptic spike. To account for modulation of synaptic current when a presynaptic cell is in an altered firing state, such as the DLAMO or DB states, we scale  $H_{\alpha}$  by a synaptic gating variable  $y_{j}(s)$  that depends on membrane voltage of presynaptic cell j and represents the fraction of activated PSC receptors, as is frequently used in spiking neuron networks [20].

From the synaptic conductances  $g_{ji}(t)$  from all presynaptic neurons j to neuron i, we calculate the total synaptic conductance  $G_i(s)$  received by the postsynaptic neuron i. The resulting firing frequency of postsynaptic cell i may depend on some or all of the parameters in  $\vec{P}(t)$ , in addition to  $G_i(t)$ . The firing rate  $f_i(G_i(t), \vec{P}_i(t))$  is then computed from a biophysical, conductance-based single-neuron model. We additionally compute the synaptic gating variable  $y_i(G_i(t), \vec{P}_i(t))$  based on the membrane voltage predicted from the biophysical SCN neuron model. These variables then feed back into the model to compute model variables at the next time step.

To arrive at a time-evolving, mean-field model as described in section 2.2, we compute the means and standard deviations of the quantities described above at each time step. In particular, we compute mean synaptic conductance  $\bar{g}(t)$  and its standard deviation  $\sigma_g(t)$  from mean population firing rate  $\bar{f}(t)$  and its standard deviation  $\sigma_f(t)$ , as well as from the synaptic response function  $H_{\alpha}$  scaled by the mean synaptic gating variable  $\bar{y}(t)$ . From  $\bar{g}(t)$  and  $\sigma_g(t)$ , we use network connectivity statistics to compute the mean and standard deviation of total synaptic conductance,  $\bar{G}(t)$  and  $\sigma_G(t)$ , respectively. Assuming the form of distributions of parameters in P across the network as well as a Gaussian distribution for total synaptic conductance  $G_i(t)$ , we compute the means and standard deviations of firing frequency  $(\bar{f}(t), \sigma_f(t))$  and synaptic gating  $(\bar{y}(t), \sigma_y(t))$  from the frequency and voltage responses of the biophysical model for individual neurons in the network.

**2.1. Computing neural firing rates.** To model the postsynaptic response of a neuron to a presynaptic spike, we let  $g_0$  be the maximum synaptic conductance and assume synaptic

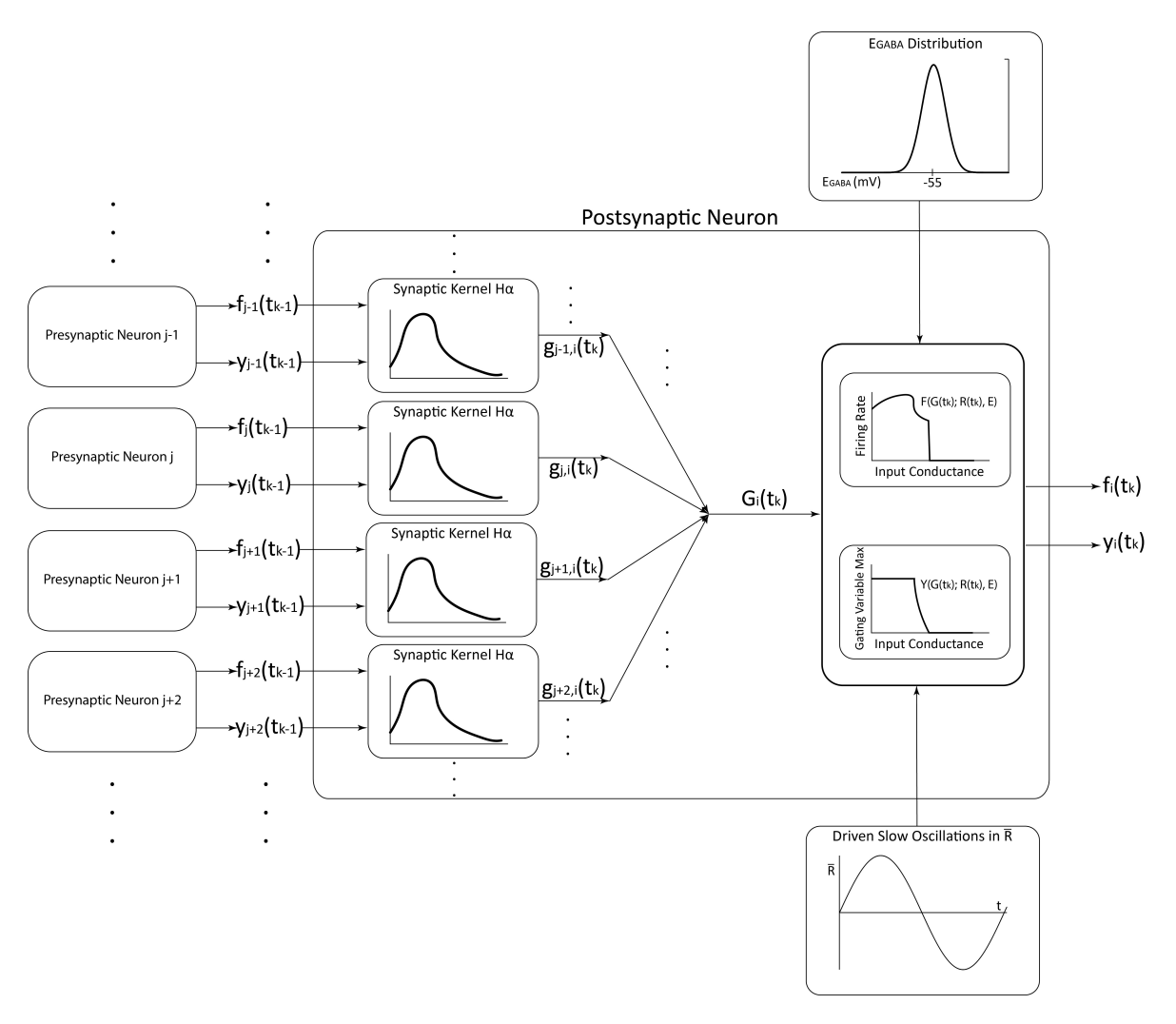


Figure 1. Schematic of model algorithm for computing the postsynaptic neuron response. Postsynaptic neuron i (large rectangle) receives synaptic inputs from multiple presynaptic neurons j as determined by the network structure. The conductance of the postsynaptic current  $g_{j,i}(t)$  induced by presynaptic cell j firing  $f_j(t)$  is modeled by its convolution with the synaptic response function  $H_{\alpha}$  scaled by the synaptic current gating variable  $y_j(t)$ . We assume linear temporal summation of synaptic conductances. Postsynaptic firing rate and maximum synaptic gating variable of neuron i at time  $t_k$ ,  $f_i(t_k)$  and  $y_i(t_k)$ , respectively, are computed from a biophysical SCN neuron model and synaptic gating functions which depend on parameters  $\vec{P}(t_k)$ . Illustrated here in the case of the SCN,  $\vec{P}$  consists of a circadian phase proxy parameter called R (see section 3) and GABA reversal potential  $E_{GABA}$ .

currents are governed by an  $\alpha$  function (see [20]). We define the synaptic response function  $H_{\alpha}(t)$  as

(2.1) 
$$H_{\alpha}(t) = \begin{cases} g_0 \frac{t}{\tau} e^{1-t/\tau}, & t \ge 0, \\ 0, & t < 0, \end{cases}$$

where time constant  $\tau$  determines the duration of the synaptic response. However, to allow for variations in synaptic conductance based on potentially altered presynaptic cell firing states, we scale  $g_0$  by a synaptic gating variable. This synaptic gating variable for presynaptic cell j,  $y_j(t)$ , depends on cell j's firing rate  $f_j(t)$  which, in turn, depends on the total synaptic conductance  $G_j(t)$  that cell j receives as well as the parameter values for cell j,  $\vec{P}_j(t)$ . Thus, PSC conductance due to firing activity in presynaptic cell j is described by

$$y_j(G_j(t), \vec{P}_j(t)) \cdot H_{\alpha}(t).$$

**2.1.1. Synaptic conductance** (g). Continuing from above, for postsynaptic cell i, the time-dependent conductance of synaptic current induced by presynaptic cell j firing at time s is modeled as

$$g_{ji}(t) = y_j(G_j(s), \vec{P}_j(s)) \cdot H_\alpha(t-s).$$

Assuming linear temporal summation of conductances due to multiple presynaptic spikes, the synaptic conductance due to all spikes from presynaptic neuron j in the small time interval  $(s, s + \Delta s)$  is

$$g_{ji}(t) \approx y_j(G_j(s), \vec{P}_j(s)) \cdot H_{\alpha}(t-s) \cdot \#\text{spikes fired}$$
  
=  $y_j(G_j(s), \vec{P}_j(s)) \cdot H_{\alpha}(t-s) \cdot f_j(G_j(s), \vec{P}_j(s)) \Delta s$ .

Dividing [0,t] into n equal intervals with left endpoints  $s_0, s_1, \ldots, s_{n-1}$ , we obtain that

$$g_{ji}(t) \approx \sum_{k=0}^{n-1} y_j(G_j(s_k), \vec{P}_j(s_k)) \cdot H_\alpha(t-s_k) \cdot f_j(G_j(s_k), \vec{P}_j(s_k)) \Delta s.$$

Letting  $\Delta s \to 0$  gives the synaptic conductance  $g_{ji}(t)$  in postsynaptic neuron i induced from firing of presynaptic neuron j as

(2.2) 
$$g_{ji}(t) \approx \int_0^t H_{\alpha}(t-s) \cdot y_j(G_j(s), \vec{P}_j(s)) \cdot f_j(G_j(s), \vec{P}_j(s)) ds.$$

$$(2.3) = (H_{\alpha} \star y_i f_i)(t).$$

**2.1.2. Total synaptic conductance** (G) in a postsynaptic neuron. To obtain the total synaptic conductance, we treat the system of synaptic inputs to a postsynaptic neuron i as a parallel circuit. Hence, we have linear summation of conductances, and the total synaptic conductance  $G_i$  in postsynaptic neuron i is

(2.4) 
$$G_i(t) = \sum_{j=1}^n g_{ji}(t),$$

where n is the total number of presynaptic cells.

**2.1.3.** Neuron firing rate (f) and synaptic gating (y). From the total synaptic conductance  $G_i(t)$ , along with the neuron-dependent parameters  $\vec{P}_i(t)$ , we model the neuronal firing rate of postsynaptic neuron i as a deterministic function F of  $(G_i(t), \vec{P}_i(t))$ :

(2.5) 
$$f_i(t) = F(G_i(t), \vec{P}_i(t)).$$

F is computed from a biophysical conductance-based model for the individual neurons in the network of the form

(2.6) 
$$C_i \frac{dV_i}{dt} = I_{syn,i} - I_{ion,i},$$

where  $C_i$ ,  $V_i$ ,  $I_{syn,i}$ , and  $I_{ion,i}$  describe the capacitance of the cell membrane, the voltage across the cell membrane, the incoming current via synapses with other neurons, and the membrane ionic currents, respectively, for the *i*th neuron (see section 3 for SCN neuron model). Synaptic input is modeled by the synaptic current  $I_{syn,i}$  which for postsynaptic cell *i* is given by

$$I_{syn,i}(t) = G_i(t) \cdot (E_{syn,i} - V_i(t)).$$

To compute the function F, the neuron model is numerically integrated across appropriate ranges of G and  $\vec{P}$  values, and the value of F is set to the firing frequency of the stationary solution (obtained when numerical integration reaches a periodic orbit or steady state). We note that since the firing rate is assigned based on the stationary response to  $G_i(t)$ , there is the underlying assumption that  $G_i(t)$  varies sufficiently slowly so that any transient behavior is negligible.

The synaptic gating variable  $y_i(t)$  for neuron i is defined by the deterministic function Y that depends on the same variables and parameters that affect firing rate

(2.8) 
$$y_i(t) = Y(G_i(t), \vec{P}_i(t)).$$

To compute Y, the model equations for the synaptic gating variable  $\hat{y}(t)$  are numerically integrated in conjunction with the neuron model across the ranges of G and  $\vec{P}$  values (see section 3 for the model used in the SCN network). The synaptic gating function Y is then set to the maximum value of  $\hat{y}(t)$  obtained in the stable solution:

(2.9) 
$$Y(G, \vec{P}) = \max_{V} \{\hat{y}(V(t); G, \vec{P})\}.$$

- **2.2. Computing statistics of network firing rate.** To construct the model for the population firing rate of the network, we calculate averages and standard deviations for synaptic conductance and firing rate variables across all neurons in the network, accounting for distributions in the parameters  $\vec{P}(t)$ . To do so, we treat these variables, such as g, G,  $\vec{P}$ ,  $N_{syn}$  f, and yf, as random quantities drawn from (potentially time-varying) distributions. The distributions for each variable are fixed across all synapses and neurons in the network.
- **2.2.1. Statistics for firing rate** (f) and synaptic gating (y). Since firing rate depends on total synaptic conductance G as well as  $\vec{P}$ , its mean across the SCN network and its standard deviation depend on the distributions of those variables and parameters in the network. Viewing  $G, \vec{P}$  together as a (1+m)-dimensional stochastic process  $(G(t), \vec{P})$ , denote the joint distribution at time t of G(t) and  $\vec{P}$  by  $\gamma_t(\vec{x})$ , where  $\vec{x}$  represents a particular value of  $(G(t), \vec{P}(t))$ . Letting  $U = \mathbb{R}^{1+m}$ , the mean firing rate  $\overline{f}(t)$  and its standard deviation  $\sigma_f(t)$  are computed as

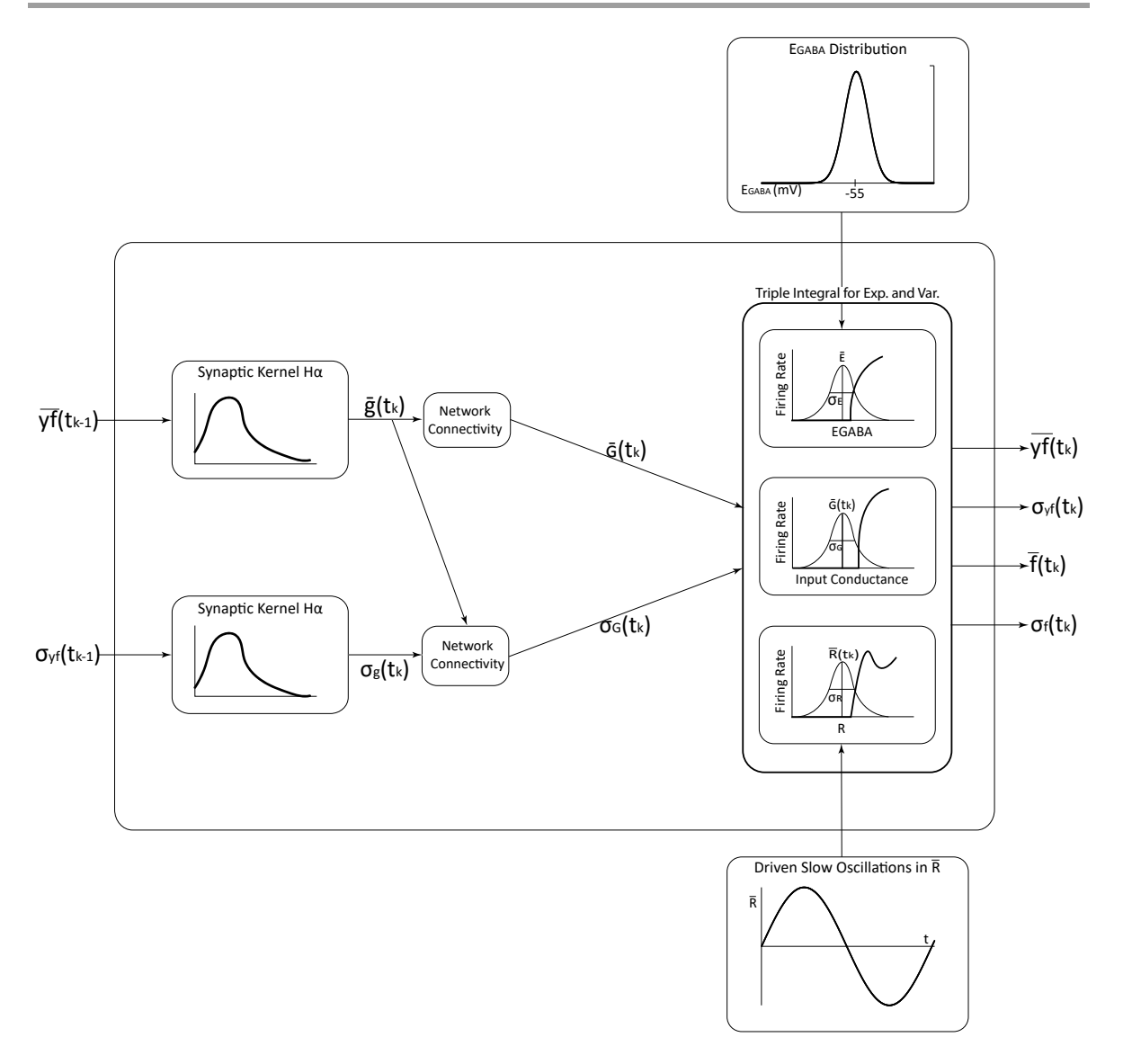


Figure 2. Schematic of model algorithm for computing network averages and standard deviations of synaptic conductances and firing rate variables. Mean firing rate scaled by synaptic gating  $\overline{yf}(t_{k-1})$  and its standard deviation  $\sigma_{yf}(t_{k-1})$  at the (k-1)th step are convolved with the synaptic kernel  $H_{\alpha}$  to yield the mean synaptic conductance  $\overline{g}(t_k)$  and standard deviation  $\sigma_g(t_k)$  at the kth time step. Applying network connectivity statistics yields the mean total synaptic conductance  $\overline{G}(t_k)$  and its standard deviation  $\sigma_G(t_k)$ . A uniform distribution for G along with the defined distributions for  $\vec{P}$  form the joint distribution for  $(G, \vec{P})$ . This joint distribution is then used to calculate the expectations  $\overline{f}(t_k)$ ,  $\overline{y}(t_k)$  of the firing rate and the synaptic gating, respectively, as well as their standard deviations  $\sigma_f(t_k)$  and  $\sigma_y(t_k)$ . To provide a concrete example, here we take  $\vec{P}$  to represent the parameters constituting  $\vec{P}$  in the SCN model (see section 3): the circadian proxy R and the GABA reversal potential  $E_{GABA}$ .

(2.10) 
$$\overline{f}(t) = \int_{U} F(\vec{x}) \gamma_t(\vec{x}) d\vec{x},$$

(2.10) 
$$\overline{f}(t) = \int_{U} F(\vec{x}) \gamma_{t}(\vec{x}) d\vec{x},$$
(2.11) 
$$\sigma_{f}^{2}(t) = \int_{U} [F(x, y, z) - \overline{f}(t)]^{2} \gamma_{t}(\vec{x}) d\vec{x}.$$

Similarly, the mean and standard deviation of the product, yf(t), of firing rate f(t) and synaptic gating y(t), is computed as

(2.12) 
$$\overline{yf}(t) = \int_{U} YF(\vec{x})\gamma_{t}(\vec{x})d\vec{x},$$

(2.13) 
$$\sigma_{yf}^2(t) = \int_U [YF(\vec{x}) - \overline{yf}(t)]^2 \gamma_t(\vec{x}) d\vec{x}.$$

**2.2.2. Statistics for synaptic conductance** g. The mean synaptic conductance  $\overline{g}$  and its standard deviation  $\sigma_g$  across all neurons are computed using the following equations with the derivations given below:

(2.14) 
$$\overline{g}(t) = (H \star \overline{yf})(t) := \int_0^t H(t-s)\overline{yf}(s)ds,$$

(2.15) 
$$\sigma_g(t) = (H \star \sigma_{yf})(t) := \int_0^t H(t-s)\sigma_{yf}(s)ds,$$

where we assume each  $g_{i,j}$  is drawn from the same distribution across all synapses. The  $\overline{g}(t)$  equation is derived by using the Tonelli–Fubini theorem [24] to pass the expectation through the integral in (2.2):

$$\overline{g}(t) = \mathbb{E}\left[\int_0^t H(t-s) \cdot y f(s) ds\right]$$
$$= \int_0^t H(t-s) \mathbb{E}\left[y f(s)\right] ds$$
$$= \int_0^t H(t-s) \cdot \overline{y f}(s) ds.$$

The derivation of the  $\sigma_g(t)$  equation, on the other hand, is more complicated. Namely, it is true if the autocorrelation coefficient  $\rho_{yf}(s_1, s_2) \approx 1$ , as shown by [55]. Indeed, following the derivation from [55], rewriting the variance using the normalized autocorrelation coefficient of yf(t) at times  $s_1$  and  $s_2$ ,  $\rho_{yf}(s_1, s_2)$ , we have that

$$Var(H \star yf)(t) = \mathbb{E}\left[\int_0^t H(t-s) \cdot yf(s)ds - \int_0^t H(t-s) \cdot \overline{yf}(s)ds\right]^2$$

$$= \mathbb{E}\left[\int_0^t H(t-s) \cdot (yf(s) - \overline{yf}(s))ds\right]^2$$

$$= \mathbb{E}\left[\int_0^t H(t-s_1)(yf(s_1) - \overline{yf}(s_1))ds_1 \int_0^t H(t-s_2)(yf(s_2) - \overline{yf}(s_2))ds_2\right]$$

$$= \mathbb{E}\left[\int_{0}^{t} \int_{0}^{t} H(t-s_{1})H(t-s_{2}) \cdot (yf(s_{1}) - \overline{yf}(s_{1}))(yf(s_{2}) - \overline{yf}(s_{2}))ds_{1}ds_{2}\right]$$

$$= \int_{0}^{t} \int_{0}^{t} H(t-s_{1})H(t-s_{2}) \cdot \mathbb{E}\left[(yf(s_{1}) - \overline{yf}(s_{1}))(yf(s_{2}) - \overline{yf}(s_{2}))\right]ds_{1}ds_{2}$$

$$= \int_{0}^{t} \int_{0}^{t} H(t-s_{1})H(t-s_{2}) \cdot \rho_{yf}(s_{1},s_{2})\sigma_{yf}(s_{1})\sigma_{yf}(s_{2})ds_{1}ds_{2}.$$

The convolution integral, however, only depends on the last few seconds because for  $t-s \ge 2$  seconds, H(t-s) is on the order of machine precision. But, assuming circadian phase varies slowly (on the scale of hours), yf should vary slowly enough that it is approximately constant on the scale of the convolution integral. Therefore, the autocorrelation coefficient  $\rho_{yf}(s_1,s_2) \approx 1$  for times  $s_1,s_2$  within about 2 seconds of one another, and thus

$$Var(H \star yf) \approx \int_{0}^{t} \int_{0}^{t} H(t - s_{1})H(t - s_{2})\sigma_{yf}(s_{1})\sigma_{yf}(s_{2})ds_{1}ds_{2}$$

$$= \int_{0}^{t} H(t - s_{1})\sigma_{yf}(s_{1})ds_{1} \int_{0}^{t} H(t - s_{2})\sigma_{yf}(s_{2})ds_{2}$$

$$= \left(\int_{0}^{t} H(t - s)\sigma_{yf}(s)ds\right)^{2},$$

which yields (2.15).

For computational simplicity, we rewrite the convolution integrals (2.14) and (2.15) as differential equations:

(2.16) 
$$\overline{g}'' = -2\tau^{-1}\overline{g}' - \tau^{-2}\overline{g} + \tau^{-1}eg_0\overline{y}\overline{f}(t),$$

(2.17) 
$$\sigma_g'' = -2\tau^{-1}\sigma_g' - \tau^{-2}\sigma_g + \tau^{-1}eg_0\sigma_{yf}(t).$$

The veracity of these differential equations is easily checked (see Appendix E).

**2.2.3. Statistics for total synaptic conductance** (G). From the statistics for synaptic conductance g, we calculate total synaptic conductance  $G_i$  of neuron i by treating it as the compound random variable  $G_i = \sum_{j=1}^{N_{syn,i}} g_{j,i}$ , where  $N_{syn,i}$  is the number of incoming synaptic connections and  $g_{j,i}$  is the conductance induced at the synapse in neuron i by the jth synaptic connection. Then, if we assume  $N_{syn,i}$  and  $g_{j,i}$  to be uncorrelated for all synapses  $j = 1, \ldots, N_{syn,i}$  incoming into neuron i, we have

$$\overline{G}(t) = \overline{N}_{syn}\overline{g}(t),$$

where  $\overline{N_{syn}}$  is the average number of incoming synapses to a neuron across the network.

To compute the standard deviation,  $\sigma_G(t)$ , of the total synaptic conductance, we assume that  $g_{j,i}(t)$  for all  $j = 1, ..., N_{syn,i}$  are pairwise conditionally uncorrelated with one another given  $N_{syn,i}$ . This means that for all i, j, l,

(2.19) 
$$\mathbb{E}[g_{j,i}g_{l,i}|N_{syn,i}] = \mathbb{E}[g_{l,i}|N_{syn,i}]\mathbb{E}[g_{j,i}|N_{syn,i}].$$

We further need to assume that  $g_{j,i}(t)$  for all  $j=1,\ldots,N_{syn,i}$  are independent of  $N_{syn,i}$ . Or, more simply we could replace these two assumptions with the stronger assumption that  $g_{j,i}(t)$  for all  $j=1,\ldots,N_{syn,i}$  and  $N_{syn,i}$  form a mutually independent collection of random variables. In either case, it suffices to calculate the mean and variance of G for a single neuron, and we have from the law of total variance that

$$\begin{split} Var[G] &= \mathbb{E}\left[Var(G_i|N_{syn,i})] + Var\left(\mathbb{E}\left[G_i|N_{syn,i}\right]\right) \\ &= \mathbb{E}\left[Var\left(\sum_{j=1}^{N_{syn,i}} g_{j,i}|N_{syn,i}\right)\right] + Var\left(\mathbb{E}\left[\sum_{j=1}^{N_{syn,i}} g_{j,i}|N_{syn,i}\right]\right) \\ &= \mathbb{E}\left[\sum_{j=1}^{N_{syn,i}} Var\left(g_{j,i}|N_{syn,i}\right) + \sum_{j=1;j\neq l}^{N_{syn,i}} \left(\mathbb{E}[g_{j,i}g_{l,i}|N_{syn,i}] - \mathbb{E}[g_{l,i}|N_{syn,i}]\mathbb{E}[g_{j,i}|N_{syn,i}]\right)\right] \\ &+ Var\left(\sum_{j=1}^{N_{syn,i}} \mathbb{E}\left[g_{j,i}|N_{syn,i}\right]\right), \end{split}$$

where we use the definition of the variance to expand and simply the first term on the right-hand side. Using (2.19) to further simplify the first term on the right-hand side above, and using the independence of  $g_{j,i}(t)$  and  $N_{syn,i}$  for all  $j = 1, ..., N_{syn,i}$  to remove the conditionality, we have that

$$Var[G] = \mathbb{E}\left[\sum_{j=1}^{N_{syn,i}} Var\left(g_{j,i}|N_{syn,i}\right)\right] + Var\left(\sum_{j=1}^{N_{syn,i}} \mathbb{E}\left[g_{j,i}|N_{syn,i}\right]\right)$$
$$= \mathbb{E}\left[\sum_{j=1}^{N_{syn,i}} Var\left(g_{j,i}\right)\right] + Var\left(\sum_{j=1}^{N_{syn,i}} \mathbb{E}\left[g_{j,i}\right]\right).$$

Assuming that each  $N_{syn,i}$  is drawn from the same distribution, just as we have assumed for each  $g_{j,i}$ , we can drop the subscripts from the preceding calculation, obtaining that

$$Var[G] = \mathbb{E}\left[N_{syn}\sigma_g^2\right] + Var\left(N_{syn}\overline{g}\right)$$
$$= \sigma_g^2 \mathbb{E}\left[N_{syn}\right] + \overline{g}^2 Var\left(N_{syn}\right),$$

and thus obtaining the expression for the variance of G as appears in [55]:

(2.20) 
$$\sigma_G^2(t) = Var(N_{syn})(\overline{g}(t))^2 + \overline{N_{syn}}\sigma_g^2(t).$$

While (2.18) and (2.20) give the statistics needed for our model algorithm, the preceding discussion does not specify the shape of the distribution beyond its first and second moments. However, if  $\overline{N_{syn}}$  is large and  $Var(N_{syn})$  is small, then  $N_{syn,i} \approx N >> 0$ , some large constant for all neurons i, and we can invoke the central limit theorem to conclude that G is roughly normally distributed. If, on the other hand, such conditions fail to hold, yet the distributions of g and  $N_{syn}$  are known, one may instead obtain the shape of the distribution of G in terms of its characteristic function  $\phi_G$  (see Appendix C).

**2.2.4.** Joint distribution of  $(G, \vec{P})$ . We have now discussed how one may find the marginal distribution of  $(G, \vec{P})$  with respect to G, but to define (2.10)–(2.13), one must determine the full joint distribution  $\gamma_t(\vec{x})$  of the stochastic process  $(G(t), \vec{P}(t))$  at time t. To do so, we assume that G, and the parameters  $P_1, P_2, \ldots, P_M$  constituting  $\vec{P}$ , are independent (see further comments in the Discussion). Hence, the joint probability distribution function  $\gamma_t$  at time t is

(2.21) 
$$\gamma_t(\vec{x}) = PDF_{G(t)}(x_1) \cdot PDF_{P_1(t)}(x_2) \dots PDF_{P_m}(x_{m+1}),$$

where  $PDF_{X(t)}(\cdot)$  represents the probability density function at time t of a stochastic process X(t) for which the random variable  $X_t$  is defined by  $X_t = X(t)$  with mean  $\overline{X}(t)$  and standard deviation  $\sigma_X(t)$  at time t.

A summary of our mean-field firing-rate model is given in section 2.3, below.

**2.3. Model summary.** Evolve synaptic conductance statistics  $\overline{g}(t)$  and  $\sigma_g(t)$  as per (2.16)–(2.17):

$$\overline{g}'' = -2\tau^{-1}\overline{g}' - \tau^{-2}\overline{g} + e\tau^{-1}eg_0\overline{yf}(t),$$
  
$$\sigma_{g}'' = -2\tau^{-1}\sigma_{g}' - \tau^{-2}\sigma_{g} + \tau^{-1}eg_0\sigma_{uf}(t),$$

where  $\overline{yf}(t)$  and  $\sigma_{yf}(t)$  are given by (2.12)–(2.13):

$$\overline{yf}(t) = \int_{U} YF(\vec{x})\gamma_{t}(\vec{x})d\vec{x},$$

$$\sigma_{yf}^{2}(t) = \int_{U} [YF(\vec{x}) - \overline{yf}(t)]^{2}\gamma_{t}(\vec{x})d\vec{x},$$

and  $\vec{x}$  represents values of  $(G(t), \vec{P}(t))$ . Firing-rate statistics are obtained at each time by (2.10)–(2.11):

$$\overline{f}(t) = \int_{U} F(\vec{x}) \gamma_{t}(\vec{x}) d\vec{x},$$

$$\sigma_{f}(t) = \int_{U} [F(\vec{x}) - \overline{f}(t)] \gamma_{t}(\vec{x}) d\vec{x}.$$

Calculation of  $\overline{yf}(t)$ ,  $\sigma_{yf}(t)$ ,  $\overline{f}(t)$ , and  $\sigma_{f}(t)$  requires previous identification of

- 1. the neuronal firing rate F and the product of F and the synaptic gating Y, YF, as functions of total synaptic conductance G and parameters  $\vec{P}$ 
  - Computed by numerically integrating the single neuron model and synaptic gating equation over relevant ranges of G and  $\vec{P}$ , and linearly interpolating or fitting a polynomial to the data as appropriate.
- 2. the joint probability distribution  $\gamma_t$  of  $(G(t), \vec{P}(t))$ 
  - Assume that G and the components  $P_1(t), \ldots, P_m(t)$  of  $\vec{P}(t)$  are independent to obtain (2.21):

$$\gamma_t(\vec{x}) = PDF_{G(t)}(x_1) \cdot PDF_{P_1(t)}(x_2) \dots PDF_{P_m}(x_{m+1}).$$

• To calculate the statistics for G, make the simplifying assumptions (see section 2.2) to obtain (2.18) and (2.20):

$$\overline{G}(t) = \overline{N}_{syn}\overline{g}(t),$$

$$\sigma_G^2(t) = Var(N_{syn})(\overline{g}(t))^2 + \overline{N_{syn}}\sigma_g^2(t).$$

- **3. Applying the firing-rate model to the SCN**. We implement the mean-field firing-rate model formalism described above to simulate time-varying circadian modulation of SCN population activity. To do so, we must describe the following, as discussed below:
  - The parameters  $\vec{P}$  representing neural and synaptic characteristics that vary across the network (excluding parameters that specify network connectivity).
  - The neuronal firing rate F and the synaptic gating Y, as functions of total synaptic conductance G and parameters  $\vec{P}$ .
  - The joint distribution  $\gamma_t$  of  $(G(t), \vec{P}(t))$

Values for parameters and quantities used to apply the model to the SCN are given in Table 2 in Appendix A, and Appendix B gives details of the numerical methods used.

3.1. Parameters  $\vec{P}$  which vary across the SCN network. As discussed in the introduction, we consider two sources of heterogeneity in the SCN network. One is heterogeneity in the GABA reversal potential of SCN neurons ( $E_{GABA}$ ) which affects the response to GABAergic synaptic input. For simplicity, we assume that all synaptic inputs in the SCN are GABAergic and that  $E_{GABA}$  is constant for each neuron across the circadian cycle. The other source of heterogeneity in the SCN network is the circadian phase experienced by different neurons across the SCN. To describe this circadian phase, we use the quantity R(t), which is a measure of the activity in the molecular clock of individual SCN neurons, and which varies with a 24-hour period corresponding to the circadian cycle [17].

Hence, in applying the formalism to the SCN, we define  $\vec{P}(t)$  as

(3.1) 
$$\vec{P}(t) = (R(t), E_{GABA}).$$

3.2. Neuron firing rate (F) and synaptic gating (Y) functions for the SCN network. To compute the neuron firing rate function F, we use the conductance-based SCN neuron model of Diekman et al. [17] governed by

(3.2) 
$$C\frac{dV}{dt} = I_{syn} - I_{Na} - I_K - I_{CaL} - I_{CaNonL} - I_{KCa}(R) - I_{K-leak}(R) - I_{Na-leak}.$$

This Hodgkin–Huxley-type model contains spike-generating Na<sup>+</sup> and K<sup>+</sup> currents, two inward Ca<sup>2+</sup> currents, a Ca<sup>2+</sup>-dependent K<sup>+</sup> current and Na<sup>+</sup>- and K<sup>+</sup>-mediated leak currents. This model replicates the firing responses of SCN neurons across the circadian cycle by accounting for the effects of circadian clock genes and proteins on membrane K<sup>+</sup> currents. Specifically, the circadian proxy parameter R(t) modulates the conductance of the Ca<sup>2+</sup>-dependent K<sup>+</sup> current  $I_{KCa}$  and the K<sup>+</sup>-mediated leak current  $I_{K-leak}$ . Low values of R correspond to circadian phases in the night and result in no firing or low firing rates in response to low values of input, while higher R values correspond to circadian phases in the middle of the day and can result in DLAMO firing and DB states and generally lead to higher signalling strength (Figure 3).

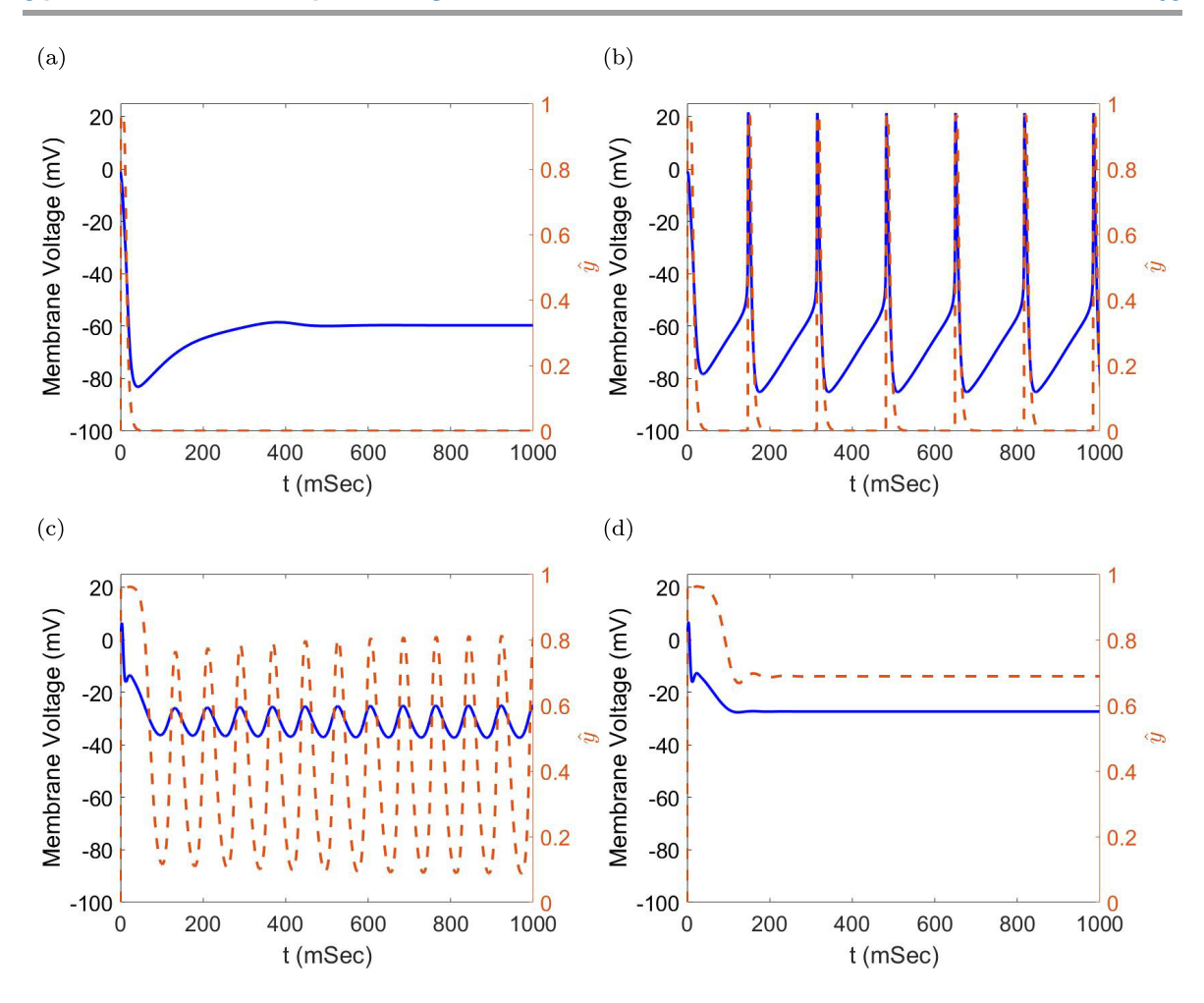


Figure 3. Diverse firing and synaptic gating behavior at different circadian phases in the biophysical SCN neuron model [17]. Voltage V(t) traces (left axes, solid blue lines) and synaptic gating  $\hat{y}(t)$  as a function of V(t) (right axes, dashed red lines) for values of the circadian proxy R and external applied current  $I_{app}$  exhibiting four firing regimes. (a) A neuron at rest, with circadian proxy R = -5 and applied current  $I_{app} = 2$   $\mu A/cm^2$ . Such behavior fails to induce postsynaptic current and is expected of SCN neurons at night [5]. (b) A neuron with R = -5 and  $I_{app} = 8$   $\mu A/cm^2$ , exhibiting typical action potential (AP) firing. Such behavior results in large synaptic gating during the AP and is expected in circadian morning and circadian evening [5]. (c) A neuron with R = 4 and  $I_{app} = 8$   $\mu A/cm^2$ , exhibiting DLAMOs, where the membrane voltage oscillates roughly sinusoidally at depolarized voltages. Such behavior decreases synaptic gating and is observed in some neurons around circadian mid-day. (d) A neuron exhibiting DB, with R = 5 and  $I_{app} = 8$   $\mu A/cm^2$ , observed in some SCN neurons in circadian afternoon [5], where membrane voltage is constant and elevated due to too much excitation, often resulting in nonzero synaptic gating.

GABAergic synaptic current is modeled as

$$I_{syn}(t) = G(t) \cdot (E_{GABA} - V(t)).$$

Synaptic gating  $\hat{y}$  is modeled as in [16, 20]:

(3.4) 
$$\frac{d\hat{y}}{dt} = a_r \cdot \frac{1}{(1 + exp(-(V(t) - (-20))/3))} \cdot (1 - \hat{y}) - a_d \cdot \hat{y},$$

where  $a_r$  and  $a_d$  characterize the rise and decay rates, respectively, of synaptic gating in response to presynaptic neuron voltage V(t). See Appendix D for full equations and parameter values.

To explicitly obtain the functions F and Y (defined by (2.9)), values of  $F(G, R, E_{GABA})$  and  $Y(G, R, E_{GABA})$  were computed for each combination of G, R, and  $E_{GABA}$  on the 201-by-201-by-201 rectangular grid for  $G \in [0,1]$ ,  $R \in [-8.5, 8.5]$ , and  $E_{GABA} \in [-110,0]$ . We did so by numerically integrating (3.2) and (3.4), holding G, R and  $E_{GABA}$  constant until the numerical solution settled down to a stationary state. Level surfaces of the resulting data  $F(G, R, E_{GABA})$ ,  $Y(G, R, E_{GABA})$  and the product  $YF(G, R, E_{GABA})$  for different values of  $E_{GABA}$  are shown in Figure 4. In this figure, boundaries between the different firing regimes—AP firing, DLAMO, DB, and resting—are indicated.

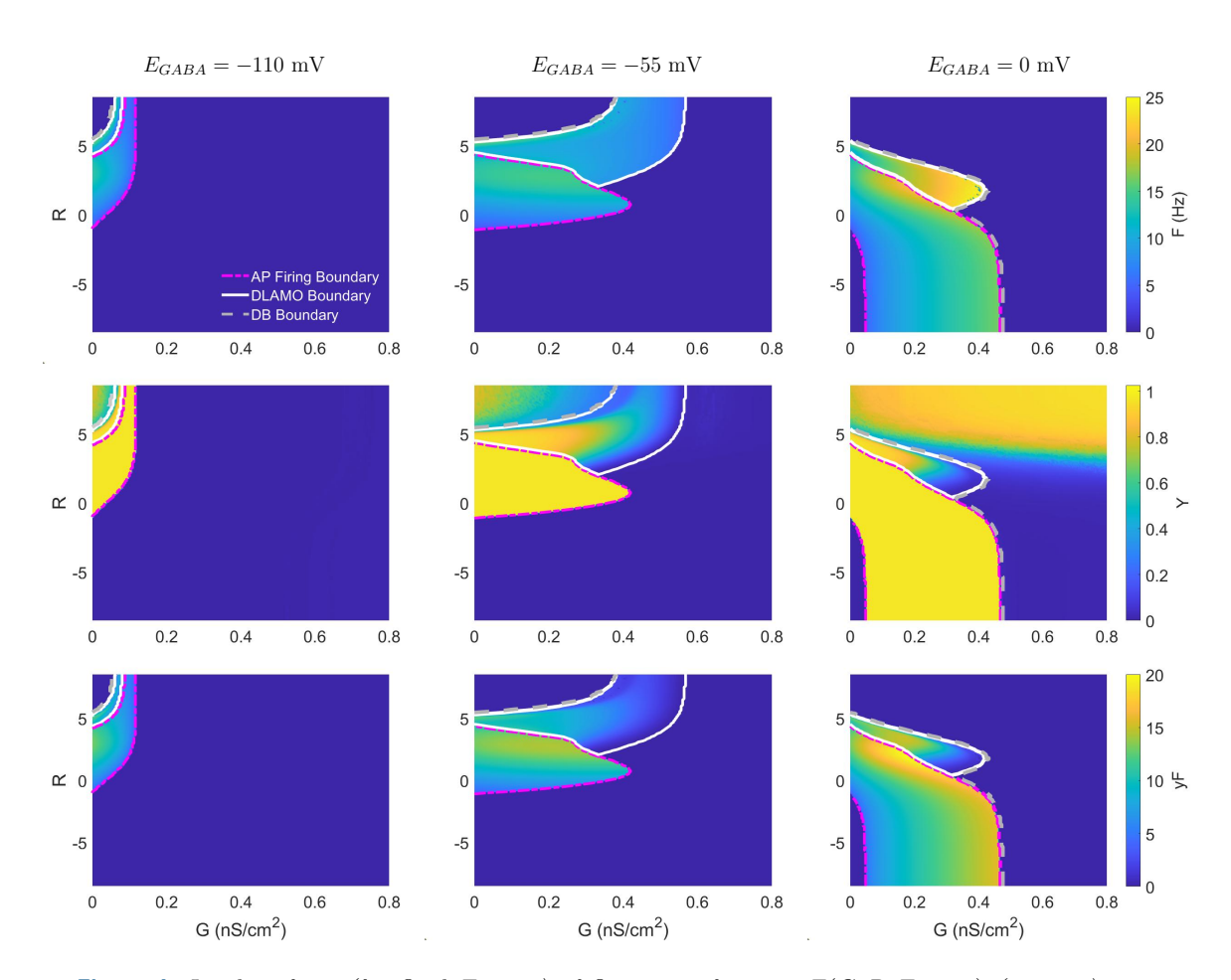


Figure 4. Level surfaces (for fixed  $E_{GABA}$ ) of firing rate function  $F(G, R, E_{GABA})$  (top row), synaptic gating function  $Y(G, R, E_{GABA})$  (middle row), and their product  $YF(G, R, E_{GABA})$  (bottom row) for  $E_{GABA} = -110$  (1st column), -55 (2nd column), and 0 mV (3rd column). Regions of each panel between magenta lines correspond to AP firing activity, whereas regions between white lines correspond to DLAMOs, regions between gray lines and the edges of the panel correspond to DB, and the remaining regions correspond to resting. Synaptic gating Y varies in these regions (row 2): in AP firing,  $Y \sim 0.965$ ; in DLAMOs,  $Y \sim 0.965$  near the boundary between AP firing and DLAMOs, but rapidly decays away from the boundary; in DB, the firing rate is zero but synaptic gating ranges from about 0 to about 0.9. When the neuron is at rest, both F and Y are zero.

Generally, higher values of  $E_{GABA}$  have a depolarizing effect on neural activity. For instance, when  $E_{GABA} = -110$  mV for all neurons in the simulation (leftmost column), synaptic currents are exclusively inhibitory, causing neurons to exit excited states such as DB, DLAMOs, and AP firing as G increases, and significantly reducing the size of (G, R) phase space in which such excited states occur. When  $E_{GABA} = -55$  mV (middle column), synaptic currents are primarily inhibitory, so that neural activity is in a resting state for high G values, but the region of (G, R) phase space corresponding to each firing regime is significantly larger. On the other hand, when  $E_{GABA} = 0$  mV (rightmost column), synaptic currents are primarily excitatory, leading to AP firing for low values of R, and to DB for sufficiently large total synaptic conductances G at all values of R. Hence, for lower values of  $E_{GABA}$ , increasing G generally increases inhibition due to synaptic currents, pushing neurons from the more excited states, DB, DLAMOs, or AP firing, to the least excited state, resting. Increasing G at higher values of  $E_{GABA}$ , on the other hand, increases excitation due to synaptic currents, having the opposite effect on neural activity.

3.3. Joint distribution for G(t), R(t), and  $E_{GABA}$  for the SCN network. To apply the model formalism to the SCN network, we write the joint probability distribution function  $\gamma_t$  at time t given by (2.21) using the parameters composing  $\vec{P}(t)$ :

$$\gamma_t(x, y, z) = PDF_{G(t)}(x) \cdot PDF_{R(t)}(y) \cdot PDF_{E_{GABA}}(z).$$

For the  $E_{GABA}$  distribution, we follow [16] and assume a normal distribution across the SCN, with a mean of -55 mV and standard deviation of 7 mV.

For the time-varying circadian proxy parameter R(t), we let R vary periodically in the range [-5,5] over a circadian period, as suggested in [16]. To model this simply, we assume that for any neuron, j, its R value,  $R_i(t)$ , varies sinusoidally, driven by circadian phase  $\theta_i(t)$ :

(3.5) 
$$R_j(t) = R_{ampl} \sin(\theta_j(t)).$$

We take each  $\theta_j(t)$  to follow a Gaussian distribution with mean  $\overline{\theta(t)}$  varying linearly over a circadian period from 0 to  $2\pi$ . In this way,  $\theta = 3\pi/2$  corresponds to the trough in circadian activity, for example. We further assume that the standard deviation  $\sigma_{\theta}$  of the Gaussian distribution is constant with respect to time. The distribution of  $R_j(t)$  is then inherited from the distribution of  $\theta_j(t)$  according to (3.5). For computational expediency, we consider a "circadian" period of about 43 seconds, as this is the minimal period needed to eliminate hysteresis in model variables across the cycle.

Finally, for the G distribution, we make the assumptions under which (2.20) holds and G is normally distributed with mean and standard deviation given by (2.18) and (2.20), respectively. To use such equations, though, we must calculate the mean  $\overline{N}_{syn}$  and variance  $Var(N_{syn})$  of the number of presynaptic neurons impinging on each neuron. To carry out the calculation, we use that the SCN has roughly 20,000 neurons [1], N = 10,000 per hemisphere. We also use that there are about  $3 - 12 \cdot 10^6$  [25] synaptic connections per SCN half, with [39] putting the number of synapses closer to the higher end of that range at  $11 \cdot 10^6$ . Further, since each synaptic connection represents 1 outgoing connection (from the presynaptic neuron) and

1 incoming connection (to the postsynaptic neuron), there are 11,000,000 incoming synaptic connections, and the average number of incoming synapses for SCN neurons should be

$$\overline{N_{syn}} = \frac{\# \text{Incoming Synaptic Connections}}{\# \text{Neurons}} = 1{,}100.$$

We recognize that some recent studies such as [47] suggest that  $\overline{N_{syn}}$  should be closer to 10. Nevertheless, we have opted to use  $\overline{N_{syn}} = 1{,}100$  until a consensus in the SCN community has been reached, noting that a reduction in  $N_{syn}$  leads to similar results after compensating by making a proportional increase in coupling strength  $g_0$ .

In any case, to use (2.20) for the variance of G, observe that if the SCN were to be modeled as a Poisson random graph with probability that any two neurons share a synapse being  $p = \overline{N_{syn}}/N = 0.11$ , then via basic properties of expectations and variances,

$$Var(N_{syn}) = \overline{N_{syn}} \cdot (p - p^2) = 979.$$

On the other hand, if, for instance, the number of incoming synapses to SCN neurons follows a pure exponential distribution  $p_k = (1 - r)^k r$ , where 1 > r > 0 is an unspecified constant, then

$$\overline{N_{syn}} = 1/r,$$

$$Var(N_{syn}) = (1 - r)/r^2 = \overline{N_{syn}}^2 (1 - 1/\overline{N_{syn}}) = \overline{N_{syn}}^2 - \overline{N_{syn}},$$

and hence if  $\overline{N_{syn}} = 1{,}100,$ 

$$Var(N_{syn}) \approx 1{,}100^2.$$

 $Var(N_{syn})$  is also  $\approx 1{,}100^2$  if the underlying distribution is log-normal, a common assumption for cortical brain areas [9]. We explore the effects of changing  $Var(N_{syn})$  in section 4.2.

- 4. Results. Here we present numerical results for our mean-field firing-rate model applied to the SCN network, considering variation of different neural and network parameters, including maximum synaptic conductance, mean and variance of synaptic reversal potentials, variance of circadian phases across the population, and variance of the number of incoming synapses per cell. We consider different amplitudes of the circadian proxy parameter R(t) to illustrate different ranges of neural activity across the circadian cycle caused by the diverse firing states of the SCN neuron model. We summarize the effects of changing these parameters on the SCN firing rate statistics in Table 1 and validate the model results against a spiking neuronal network in Appendix F.
- **4.1. Effect of changing**  $g_0$ . To investigate effects of changing maximum synaptic conductance  $g_0$ , we consider four different values of  $g_0$  (in  $\frac{mS}{cm^2}$ ):  $10^{-6}$  (very weak),  $10^{-5}$  (weak),  $10^{-4}$  (middling strength), and  $5 \cdot 10^{-4}$  (strong). To isolate the effects of  $g_0$ , we take  $E_{GABA} = -55$ mV for all neurons in the network ( $\sigma_{EGABA} = 0$ ) and let all neurons have the same circadian phase ( $\sigma_{\theta} = 0$ ) with R values that vary periodically with different amplitudes ( $R_{ampl} = 5, 3$ , and 1). We illustrate our findings in Figure 5.

Table 1

Summary of effects of various parameters on SCN network firing rate statistics across the circadian cycle. Parameters correspond to columns, the types of effects on firing rate statistics correspond to rows, and the entry in each box designates the type of correlation between the corresponding parameter and corresponding aspect of firing-rate statistics. A "+" indicates positive correlation, a "-" indicates negative correlation.

	$g_0$	$\overline{E_{GABA}}$	$Var(N_{syn})$	$\sigma_{ heta}$	$\sigma_{EGABA}$
Minimum of $\overline{f}$	- or none	– or none	- or none	+	+ or none
Maximum of $\overline{f}$	- or none	+	_	_	_
Amplitude of $\overline{f}$	Variable	Variable	Variable	_	_
Minimum of $\sigma_f$	+ or none	None	None	+	– or none
Maximum of $\sigma_f$	+ or none	+	+	+	_
Amplitude of $\sigma_f$	+	+	_	_	Variable
Amplitude of mid-day dip	_	Variable	Variable	_	+

As expected, increasing  $g_0$  from weak coupling to stronger coupling generally leads to higher mean firing rates as well as higher standard deviations in firing rates. However, for large  $R_{ampl}$  (left column) and particularly for stronger coupling, firing rates dip at peak  $\overline{R}(t)$ , the assumed circadian mid-day, due to neuronal activity entering the DLAMO region, thus leading to a decrease in synaptic signaling. For smaller  $R_{ampl}$  (middle column), firing rates plateau at "mid-day" but still dip for sufficiently large  $g_0$ , whereas for still smaller  $R_{ampl}$  values (right column), firing rates vary nearly sinusoidally, with firing rates being significantly lower for strong coupling than weaker coupling.

To clarify the process by which  $g_0$  influences firing rates, the trajectories of mean network conductance  $\overline{G}(t)$  across the R(t) cycle are plotted on the neuronal firing rate surface  $F(G, R, E_{GABA})$  (curves in panels G-I). From such plots, it is clear that maximum synaptic conductance  $g_0$  greatly affects which neuronal firing regions are sampled as R(t) varies. These plots also clarify the observed behavior of standard deviations in the firing rates. Notably, comparing panels G-I to the standard deviations in panels D-F, there is a nonzero standard deviation when the total synaptic conductances G are well above zero (see black and green curves in panels G-I). Moreover, peak standard deviations in panels D and E for stronger  $g_0$  occur when G(t) nears the boundary of firing regimes. For instance, in panels G and H, firing-rate standard deviations are large near transitions from zero to nonzero firing rates, and remain elevated until G(t) is firmly in the DLAMO regime. Further, for lowest  $R_{ampl}$ (panel I), the (G(t), R(t)) trajectory remains near the threshold for AP firing throughout the circadian cycle for strong coupling, resulting in nonzero standard deviations. These higher standard deviations arise because when we integrate over the G distribution to calculate the standard deviations of the firing rates, we integrate over the transition from action potential firing to rest.

**4.2. Effect of changing**  $Var(N_{syn})$ . Assuming a different network structure in the SCN without changing the number of neurons or synapses changes  $Var(N_{syn})$ , the variance in the number of incoming synapses per SCN neuron. In Figure 6, we consider 4 different values for  $Var(N_{syn})$  representing different network connectivity structures but assuming N = 10,000 neurons in the network and  $\overline{N_{syn}} = 1,100$  incoming synapses per neuron on

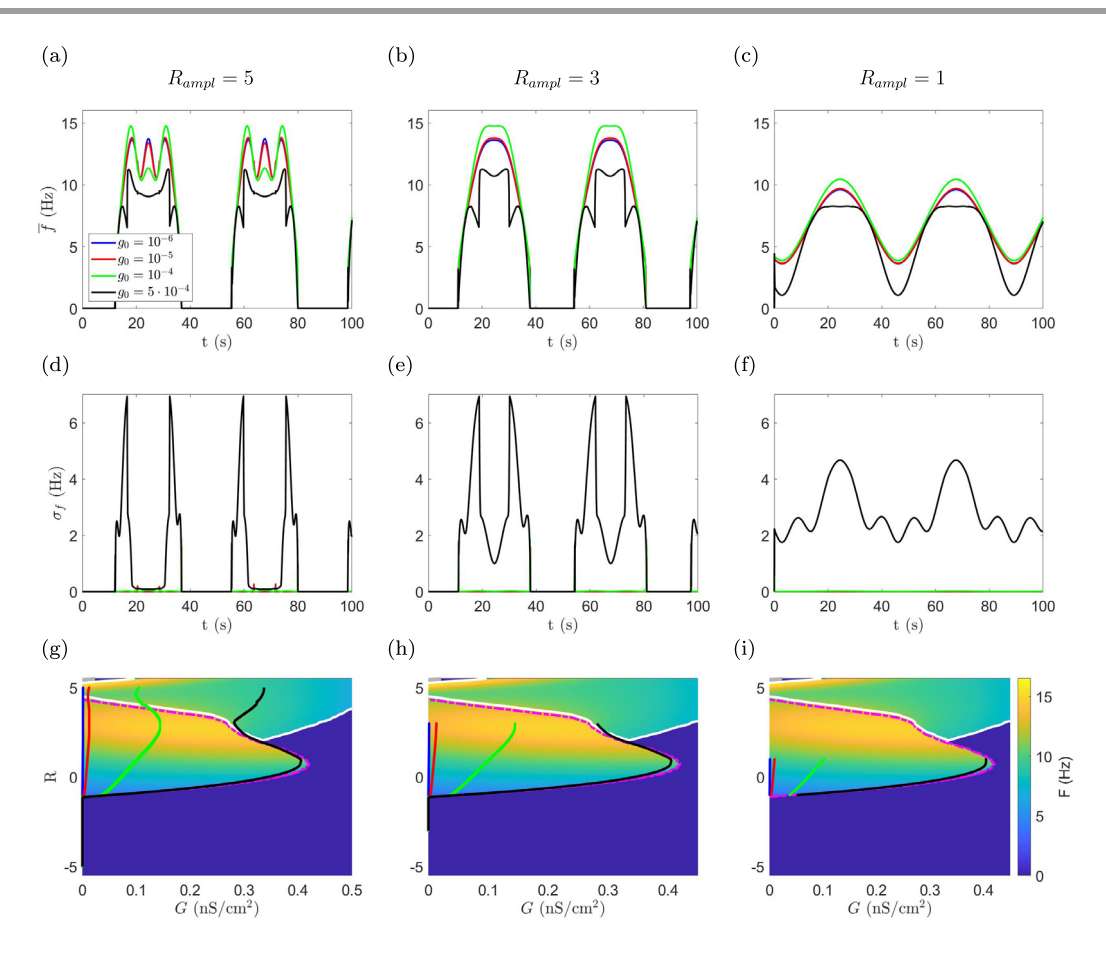


Figure 5. Effect of maximum synaptic conductance  $g_0$  on network firing rate and standard deviation. (a-f) Mean firing rates f(t) (first row) and standard deviations of firing rates  $\sigma_f(t)$  (2nd row) over multiple R(t) cycles (circadian period shortened to  $\approx 43s$ ) for 4 different values of maximum synaptic conductance  $g_0$  (in  $\frac{mS}{cm^2}$ ) ranging from strong coupling ( $g_0 = 5 \cdot 10^{-4}$ , black curves) to weak coupling ( $g_0 = 10^{-6}$ , blue curves). Three amplitudes of circadian variation are simulated,  $R_{ampl} = 5$  (left column), 3 (middle column), and 1 (right column). (g,h) ( $\overline{G(t)}$ , R(t)) trajectories are plotted (solid lines) on the neuronal firing rate surface F(G, R, -55) for the same values of  $g_0$  as in (a-f). Dashed lines represent boundaries between firing regimes, as in Figure 4. In all panels,  $E_{GABA} = -55$  mV, and there is zero variance in circadian phase across the network.

average. Specifically we consider  $Var(N_{syn}) = 0$  representing a network where all neurons receive the same number of incoming synapses,  $Var(N_{syn}) = 979$  corresponding to a Poisson distribution in  $N_{syn}$  characteristic of Poisson random graphs,  $Var(N_{syn}) = 1.21 \cdot 10^6$  corresponding roughly to exponential or log-normal distributions for  $N_{syn}$ , and  $Var(N_{syn}) = 9.79 \cdot 10^6$  corresponding roughly to the maximum possible variance according to the inequality  $Var(N_{syn}) \leq (N_{syn,max} - \overline{N_{syn}})(\overline{N_{syn}} - N_{syn,min})$  where  $N_{syn,min}$  and  $N_{syn,max}$ , the smallest and largest possible values of  $N_{syn}$ , are 0 and 10,000, respectively. As seen in the figure, increasing  $Var(N_{syn})$  slightly reduces firing-rate amplitudes but can increase firing-rate standard deviations considerably. For example, when  $R_{ampl} = 5$ , increasing  $Var(N_{syn})$  from  $1.21 \cdot 10^6$  to  $9.76 \cdot 10^6$  more than doubles firing-rate standard deviations.

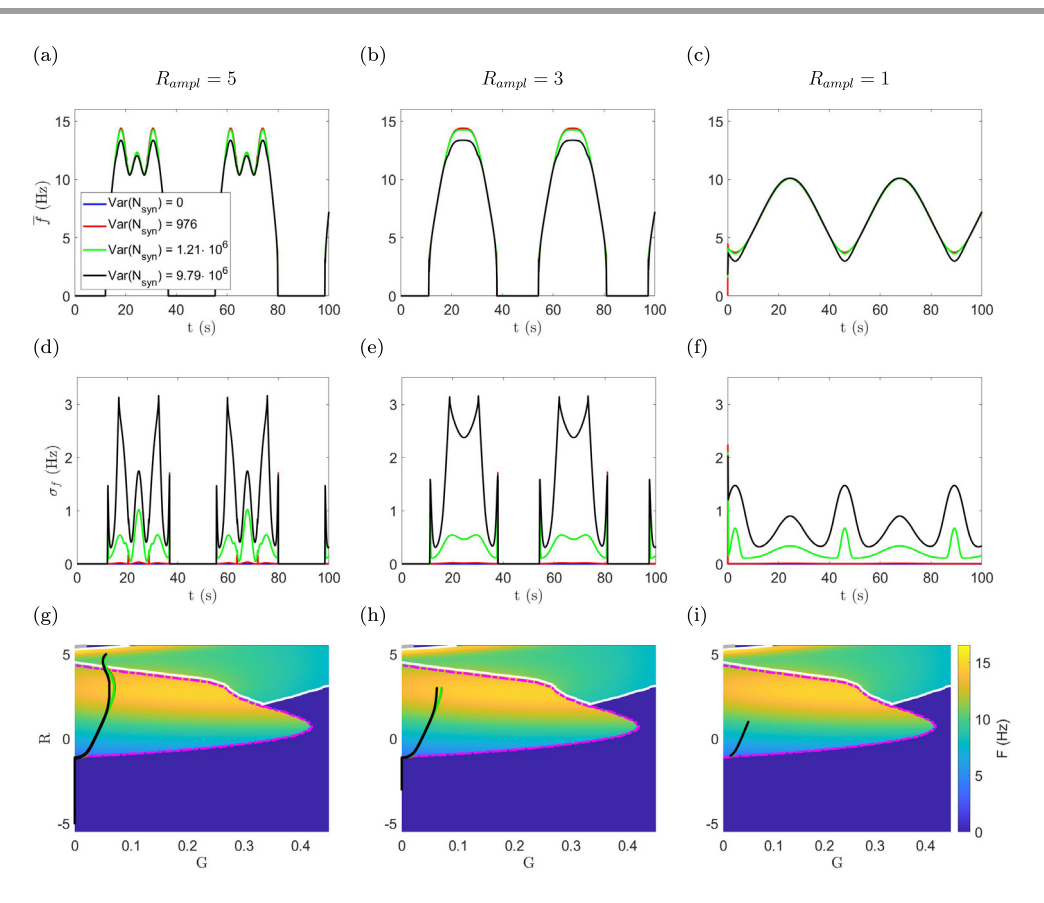


Figure 6. Effect of  $Var(N_{syn})$ , the variance in the number of presynaptic neurons per SCN neuron, on network firing rate and standard deviation given weak coupling ( $g_0 = 5 \cdot 10^{-5}$ ). (a-f) In the top row and middle row, firing rates and firing-rate standard deviations, respectively, are graphed for each of four values of  $Var(N_{syn})$ . (g,h) ( $\overline{G(t)}, R(t)$ ) trajectories are plotted (solid lines) on the neuronal firing rate surface F(G, R, -55) for the same values of  $Var(N_{syn})$  as in (a-f). Dashed lines represent boundaries between firing regimes, as in Figure 4. The left, middle, and right columns correspond to values of 5, 3, and 1, respectively, for  $R_{ampl}$ , simulated over two shortened circadian cycles. In all panels,  $E_{GABA} = -55$  mV, and there is zero variance in both circadian phase and GABA reversal potential across the network.

4.3. Effect of circadian phase distribution. Introducing variance in the circadian phases of neurons in the SCN network results in a distribution of R values. In Figure 7, circadian phase standard deviation  $\sigma_{\theta}$  values of 0 (no variation), 0.3 (middling), 0.6 (somewhat large), and 0.9 (very large) radians are considered. Increasing  $\sigma_{\theta}$  strongly reduces the amplitude of firing-rate oscillations. Even for the largest  $R_{ampl}$ , increased  $\sigma_{\theta}$  removes the "mid-day" dip because the spread in R(t) values attenuates the influence of DLAMO and DB behaviors on overall firing rate. Additionally, increasing circadian phase standard deviation keeps firing rates above zero throughout the R(t) cycle. Standard deviations in firing rate are higher with increased  $\sigma_{\theta}$  and remain elevated throughout the circadian cycle for largest  $\sigma_{\theta}$ .

**4.4. Effect of**  $E_{GABA}$  **distribution.** From our simulations, the standard deviation in  $E_{GABA}$ ,  $\sigma_{EGABA}$ , has nonnegligible effects on firing-rate statistics mainly for large maximal synaptic conductances ( $g_0 \ge 10^{-4} \text{ nS/cm}^2$ ). However, even with strong synaptic coupling,

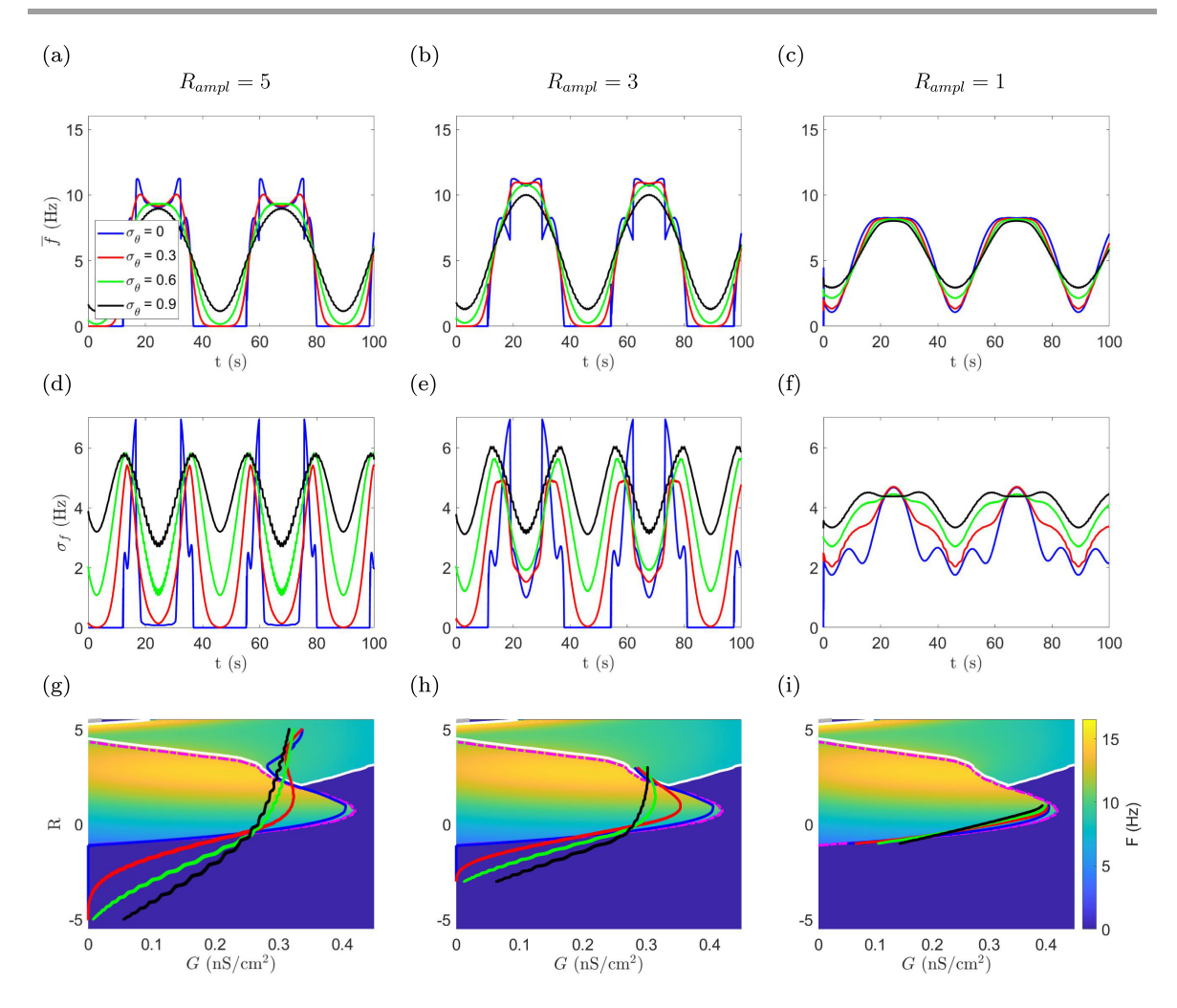


Figure 7. Effect of introducing variance in circadian phase (given  $g_0 = 5 \cdot 10^{-5} \frac{m}{cm^2}$ ,  $E_{GABA} = -55mV$ , and  $\sigma_{EGABA} = 0mV$ ). (a-f) In the top row and middle row, firing rates and firing-rate standard deviations, respectively, are graphed for each of four values of  $\sigma_{\theta}$ . (g,h)  $\overline{G(t)}$ , R(t)) trajectories are plotted (solid lines) on the neuronal firing rate surface F(G, R, -55) for the same values of  $\sigma_{\theta}$  as in (a-f). Dashed lines represent boundaries between firing regimes, as in Figure 4. The left, middle, and right columns correspond to  $R_{ampl}$  values of 5, 3, and 1, respectively, simulated over two shortened circadian cycles.

introducing a distribution in  $E_{GABA}$  only slightly dampens firing-rate oscillation amplitude (Figure 8). Indeed, as displayed in panels (a–c), firing rates corresponding to higher values of  $\sigma_{EGABA}$  have slightly lower peaks mid-day and higher troughs in the evening (for lowest  $R_{ampl}$ , right column). More visible are the changes in firing-rate standard deviation, where increasing  $\sigma_{EGABA}$  significantly increases firing-rate standard deviations especially during mid-day of the circadian cycle (panels (d–f) of Figure 8). Further simulations (not shown) attempting to isolate the effect of  $\sigma_{EGABA}$  on firing-rate statistics suggest that, particularly for weaker coupling strengths, increasing  $\sigma_{EGABA}$  primarily plays a role in increasing firing-rate standard deviations around circadian mid-day.

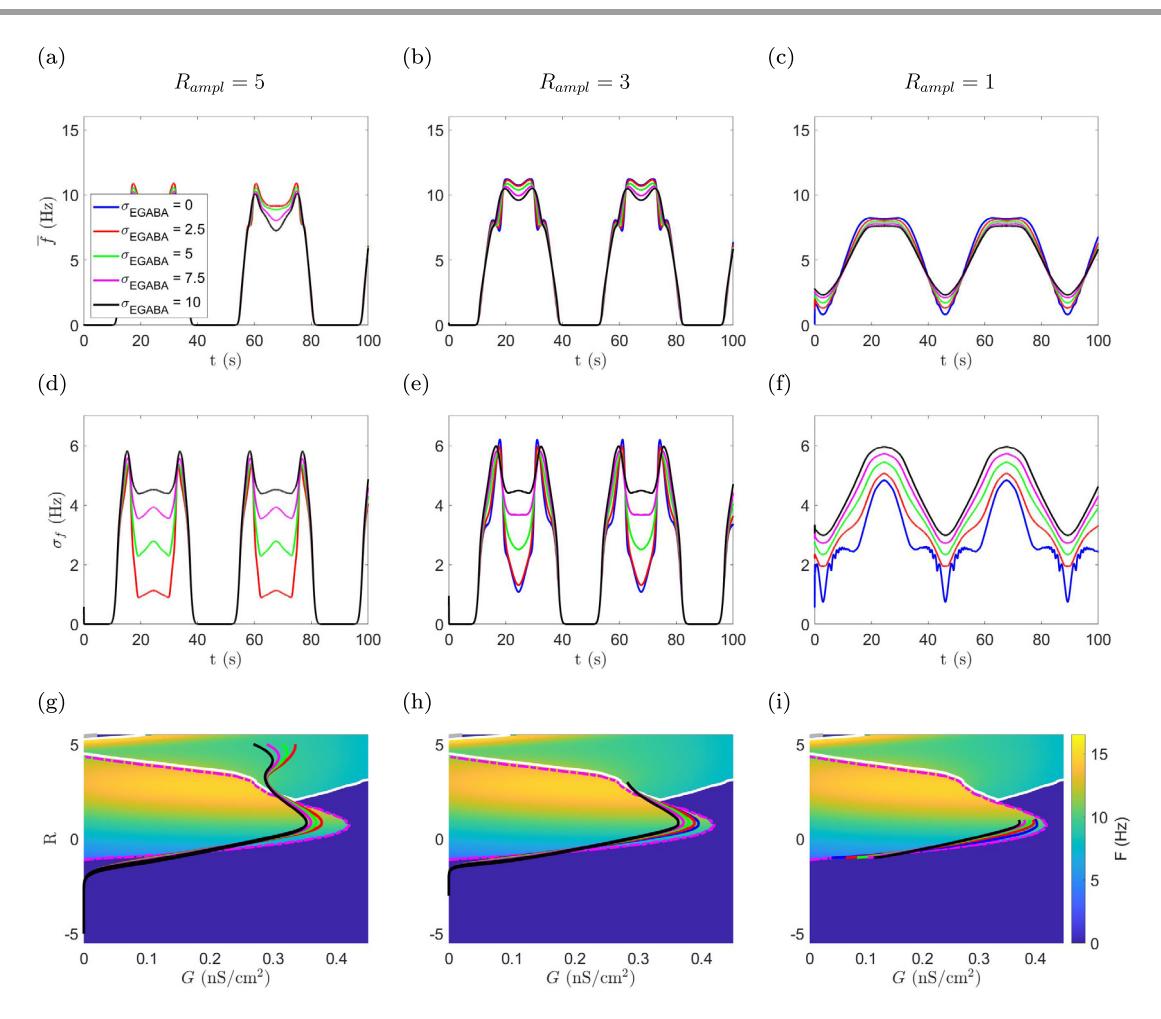


Figure 8. Effect of introducing standard deviation in  $E_{GABA}$  given strong coupling  $(g_0 = 5 \cdot 10^{-4} \frac{mS}{cm^2}, E_{GABA} = -55mV$ , and  $\sigma_{\theta} = 0.1$ ). (a-f) In the top row and middle row, firing rates and firing-rate standard deviations, respectively, are graphed for each of four values of  $\sigma_{EGABA}$ . (g,h)  $(\overline{G(t)}, R(t))$  trajectories are plotted (solid lines) on the neuronal firing rate surface F(G, R, -55) for the same values of  $\sigma_{EGABA}$  as in (a-f). Dashed lines represent boundaries between firing regimes, as in Figure 4. The left, middle, and right columns correspond to  $R_{ampl}$  values of 5, 3, and 1, respectively.

4.5. Combined effects of distributions in circadian phase and  $E_{GABA}$ . Here we consider the presumably more physiologically accurate condition where there are distributions of circadian phase and GABA reversal potential across the SCN network. Given a more realistic  $\sigma_{EGABA} = 7$  along with strong coupling  $g_0 = 5 \cdot 10^{-4}$  and some variance in  $\sigma_{\theta}$  (Figure 9), we see firing-rate oscillations qualitatively similar to those without any variance in  $E_{GABA}$  ( $\sigma_{EGABA} = 0$ ) but still with variance in circadian phase, as in Figure 7. With variance in both circadian phase and  $E_{GABA}$ , firing rates are generally several hertz lower than with only variance in  $\sigma_{\theta}$ , have means with somewhat lower peaks and higher troughs mid-day, and no secondary peaks at mid-day. Moreover, the standard deviations of firing rates are considerably larger than in Figure 7, particularly for small  $\sigma_{\theta}$  values and at mid-day in the circadian cycle.

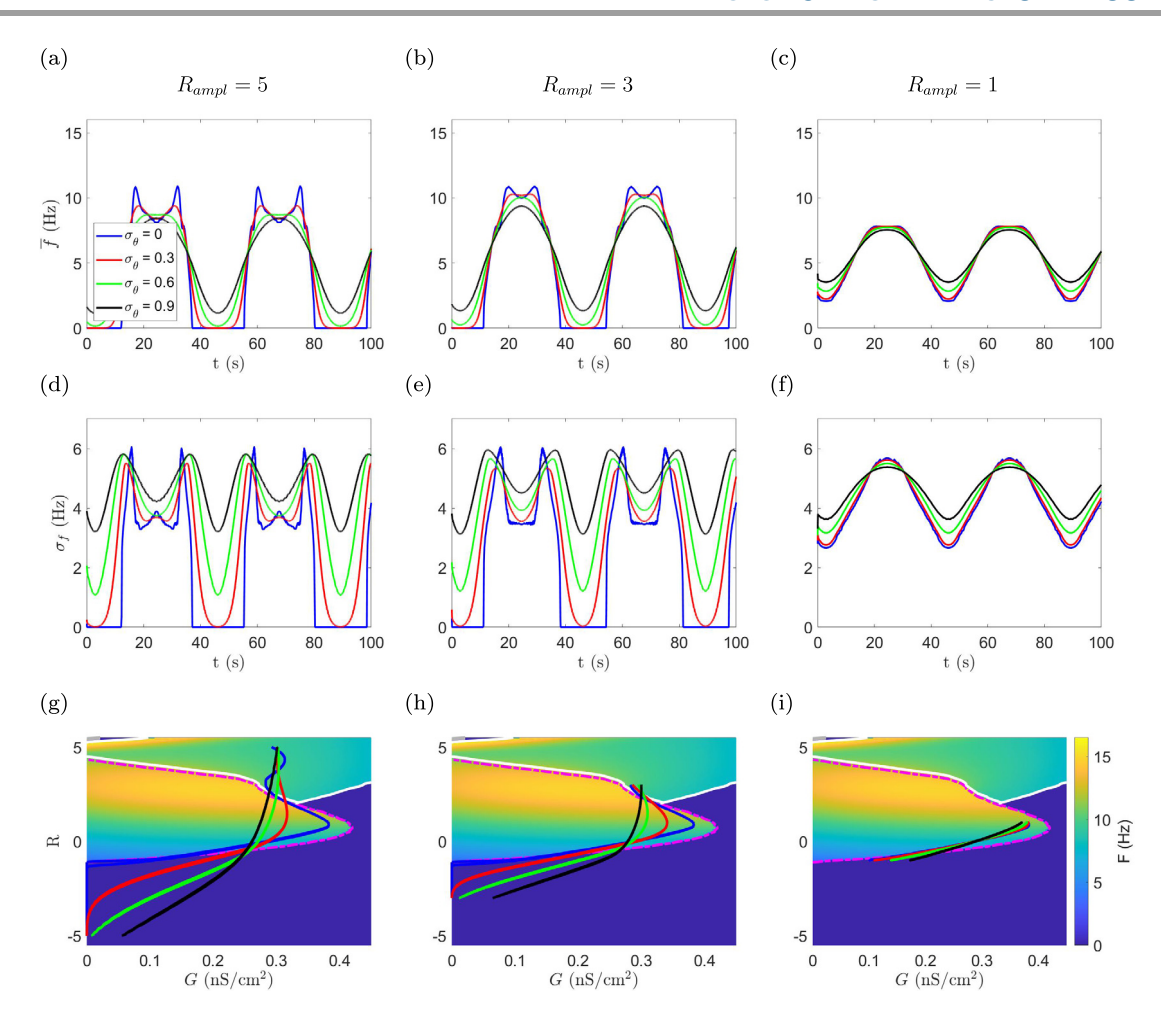


Figure 9. Role of changing variance in circadian phase given significant variance in  $E_{GABA}$  and strong coupling between neurons ( $g_0 = 5 \cdot 10^{-4} \frac{mS}{cm^2}$ ,  $\overline{E_{GABA}} = -55mV$ ,  $\sigma_{EGABA} = 7mV$ ). (a-f) In the top row and middle row, firing rates and firing-rate standard deviations, respectively, are graphed for each of four values of  $\sigma_{EGABA}$ . (g,h) ( $\overline{G(t)}$ , R(t)) trajectories are plotted (solid lines) on the neuronal firing rate surface F(G, R, -55) for the same values of  $\sigma_{EGABA}$  as in (a-f). Dashed lines represent boundaries between firing regimes, as in Figure 4. The left, middle, and right columns correspond to  $R_{ampl}$  values of 5, 3, and 1, respectively.

This suggests that while  $\sigma_{\theta}$  has larger effects on mean firing rates than does  $\sigma_{EGABA}$ , both variances increase firing-rate standard deviations, with  $\sigma_{EGABA}$  having a larger effect than  $\sigma_{\theta}$  at mid-day.

**5. Discussion.** We have introduced a mean-field firing-rate formalism for a population of neurons whose electrophysiological characteristics, such as firing responses and synaptic current reversal potentials, are modeled as probability distributions across the network. Such distributions arise in our formalism from variability in underlying network parameters, such as network connectivity, or in the case of the mammalian SCN, molecular clock phase, and GABA reversal potential. In applying the formalism to the SCN, not only have we incorporated

variation in circadian phases and GABA reversal potentials across SCN neurons, but we have incorporated into the model the unusual firing activity of SCN neurons, including DLAMOs and DB. In doing so, we have provided and illustrated an unusually flexible firing-rate model formalism which accounts for more varied and complex neuronal properties than is typical of standard firing-rate models.

5.1. Advantages of our mean-field firing-rate formalism. Indeed, the primary advantage of our model is that it allows any electrophysiological properties which can be incorporated into an underlying single-neuron model to vary roughly on a continuum across the network. In other words, our model can incorporate heterogeneity in far more diverse ways than can other firing-rate models. To start, our model allows for arbitrary degree distributions in the underlying neuronal network, that is, in the number of synapses impinging on postsynaptic neurons, thereby including the primary source of heterogeneity in firing-rate models appearing in the review [15], although our model does not include any noise terms. Further, our model expands upon the treatment of the two sources of heterogeneity appearing in the famous Wilson-Cowan model [53]. One such source of heterogeneity is that one population of neurons is excitatory while the other is inhibitory. Our model, on the other hand, by assuming varying GABAergic reversal potentials, allows PSCs to excite/inhibit postsynaptic neurons to different degrees within a single population! The other source of heterogeneity in the Wilson-Cowan model is that the firing thresholds of neurons differ. Our model also accounts for variable firing thresholds and variable types of firing activity by allowing parameters such as R and  $E_{GABA}$ underlying individual neuronal dynamics to vary. In doing so, our model also captures the heterogeneities in the "intrinsic frequencies" of neurons in Ott-Antonsen derived oscillator models appearing in [38] or [10] and expands upon this by allowing for different types of activity such as DLAMOs.

To capture all those heterogeneities, our model directly incorporates the dynamics of individual neurons through model variables and the deterministic "transfer" functions  $F(G, \vec{P})$  and  $Y(G, \vec{P})$  describing the firing-rate and gating of synaptic efficacy, respectively, for a neuron with total synaptic conductance G and parameters  $\vec{P}$ . Consequently, our model allows for the neuronal dynamics to be complex, so long as F and Y may be computed from appropriate single-neuron models. Only a few other firing-rate models have successfully incorporated complex neuronal dynamics into firing-rate models, including the convolutional model with averaging of Zandt et al. [55], the population density Fokker–Planck equation model employing Fokker–Planck equations (FPEs) [12], and the "master equation" FPE model [11].

A further advantage is that our model describes the mean and variance of firing rates of neurons across the network without attempting to calculate the full probability distribution. In this sense, our model can capture the effects of heterogeneity among neurons in the network better than models that only describe the means, such as classic firing-rate models, including "convolutional models." Describing the variance of firing-rates also informs us about the coherence of the signals output by the modeled network, which has potentially important physiological outcomes, particularly for the SCN (see section 5.2). Such descriptions are therefore lacking from models that describe only mean firing rates, including the Wilson-Cowan model [53], the heuristic but influential model of Da Silva [14], and the model of Amari [2]. Nevertheless, such convolutional models remain popular, being used to model

neurological processes in a variety of contexts, including sleep-wake dynamics [18], modeling the developing spinal cord [48], and more generally in summarizing the behavior of spiking neural networks [27].

On the other hand, there are firing-rate models which directly output both the means and standard deviations of the firing rates across the network just as our model does, of which the most relevant to this discussion is that of Zandt et al. [55]. Other models describe even more information about the variability in firing rates across the network—they describe the full probability distribution of firing rates. Such models are known as population density or FPE models. Well-known examples include the foundational model of Nykamp and Tranchina [44], the "master equation" approach of El Boustani and Destexhe [19], and those presented in the review by Deco et al. [15]. While these models provide more information about the effects of heterogeneities, they have largely not yet been used to describe heterogeneities as varied as the SCN network requires.

Despite these advantages, our model formalism does not account for varying synaptic strengths across the network. Instead, we considered a homogeneous maximum synaptic conductance  $q_0$  for all synaptic connections. Alternatively, heterogeneous synaptic strengths could be included in our formalism by considering a weighted sum for the total synaptic conductance  $G_i(t)$  in (2.4). For two cases, we can include weighted synaptic strengths directly in the derivation of the model. For the case where all outgoing synapses from a presynaptic neuron have the same weight, a scaling factor  $w_i$  can be included within the summation of (2.4). For the model derivation, the product of the synaptic gating and firing-rate functions YF(G(t), P) in (2.12) and (2.13) would be scaled by this synaptic weight and its distribution would be included in the joint distribution  $\gamma_t$  (defined in (2.21)). For the second case where all incoming synapses to a postsynaptic neuron have the same weight, a scaling factor  $w_i$  can be included within the summation of (2.4). For the model derivation, the statistics of the distribution of  $w_i$  would be incorporated into the distribution of total synaptic conductance G(t) in (2.18) and (2.20), thus modifying the distribution of G(t) in (2.21). For the case of completely heterogeneous synaptic strengths, it is possible to extend the model formalism and derive appropriate statistics for total synaptic conductance [55]. However, implementation of the model for this case would depend on the specific weighted connectivity matrix for the network.

Our model formalism also does not include a spatial component and thus cannot account for differences in firing behavior between different portions of a network of neurons. Firing-rate models which include spatial dependencies are typically called neural field models. Examples of neural field models include that of Amari [2], one of the earliest well-known neural field models, and more recently the model of wandering "bumps" by Bressloff [6]. Accounting for spatial distributions of firing rates could improve analysis of SCN network firing activity, as the SCN is divided into dorsal (shell) and ventral (core) regions, which some evidence suggests could form functionally distinct compartments within the SCN [54]. Extending our formalism to account for spatial statistics of firing rates may be considered in future work.

**5.2. Summary of effects of SCN cellular variation.** To apply our mean-field firing-rate formalism to the SCN, we have considered the scenario where SCN firing rates exhibit daily rhythmic oscillations, as observed experimentally in recordings of SCN neural activity

[8, 34, 35, 36, 50]. To generate rhythmic oscillations, we have forced periodic variation in the circadian proxy parameter R(t). However, the best time profile for R(t) to accurately simulate the effects of the molecular clock on the electrophysiological properties of SCN neurons has not been identified. Hence, we have simply modeled R(t) as sinusoidally varying. Furthermore, experimental recordings of SCN electrical activity indicate that its rhythmic oscillations can vary under different conditions, such as light intensity [3] and seasonality [50]. Thus, we have considered multiple sinusoidal time profiles for R(t) which induce the various ranges of activity levels that can be generated by the different firing states observed in the single SCN neuron model.

We have investigated the effects of variation in SCN network properties by simulating the model under a variety of values for four physiologically relevant parameters: synaptic coupling strength  $(g_0)$ , variance in the number of synapses incoming to SCN neurons  $(Var(N_{syn}))$ , standard deviation in GABA reversal potential  $(\sigma_{EGABA})$ , and standard deviation in circadian phase  $(\sigma_{\theta})$ . We have also investigated the effects of varying mean GABA reversal potential  $(\overline{E_{GABA}})$ , shown in Appendix G. The primary effects of changing these parameters are reflected in the maximum, minimum, and amplitude of oscillations of mean firing rates  $\overline{f}$  and standard deviations in firing rates  $\sigma_f$  across the simulated circadian cycle. Interestingly, we also find that parameter variation affected the occurrence of a "mid-day" dip in mean firing rates. The observed effects of these parameters on firing-rate statistics are summarized in Table 1.

Of all the observed effects on firing rates, perhaps the most physiologically significant are the effects on the amplitude of firing-rate oscillations across the circadian cycle. Indeed, our results highlight mechanisms which shrink the amplitudes of oscillations in SCN firing rates. Decreased amplitude of SCN firing-rate cycling has been observed in aged rodents [23], and would likely lead to reduced amplitude of behavioral circadian rhythms. Such blunting of behavioral circadian rhythms has likewise been associated with aging [22, 28] as well as with neurodegenerative diseases such as Alzheimer's disease [13, 31, 45] and Parkinson's Disease [13, 31, 49, 52].

Our results indicate that increasing  $\sigma_{\theta}$ , the standard deviation in circadian phases across SCN neurons, strongly decreases the amplitude of firing rates. In terms of our model, this happens because upon increasing standard deviations in circadian phase, the range of neuron firing states grows wider. Indeed, with a large standard deviation in circadian phase, in the middle of the circadian night, a typical neuron might be at rest, but other neurons whose phases correspond to earlier or later circadian times could be in the AP firing regime, thus increasing the minimum average firing rate. Similarly, lower average firing rates may occur in the middle of the circadian day due to some neurons firing at lower frequencies. Physiologically, wider standard deviations in circadian phase would correspond to desynchronization in the molecular clocks of SCN neurons. Desynchronization of gene expression rhythms in the SCN has been observed in aged rodents [43] and also in rodents in response to abrupt shifts in the light:dark cycle, as would occur with jet lag [42].

Another parameter whose growth reduced the amplitude of firing rates is  $\sigma_{EGABA}$ , the standard deviation of GABA reversal potentials across the SCN network. GABAergic neurotransmission is fundamental in the SCN [40] and consists of both synaptic GABA currents as well as extrasynaptic tonic GABA-receptor mediated currents [37]. Differences in the

locations of synaptic and extrasynaptic GABA receptors and in the local chloride concentrations may lead to differences in effective GABA reversal potentials. In our formalism, accounting for variance in  $E_{GABA}$  can reflect such diversity of GABA-mediated signaling in the network. Moreover, wider variations in  $E_{GABA}$  values lead to wider variations in synaptic signaling and thus firing responses across the network. However, large effects of  $\sigma_{EGABA}$  on mean firing rates were observed only when coupling strength between neurons was high, i.e., when total synaptic conductance was high.

While coupling strength  $g_0$  had some effect on the amplitude of oscillations in mean SCN firing rates, its effects were more nonlinear than those of other parameters. Most notable is that  $g_0$  mainly affects firing rates near circadian "mid-day." This is because the coupling  $g_0$  between two neurons only matters when the presynaptic neuron is active. Since most SCN neurons are intrinsically active at times near "mid-day," whereas few neurons are active near circadian "midnight," neuronal signaling has the largest capacity to be influenced by  $g_0$  near "mid-day." In particular, for low values of  $g_0$ , mean firing rates show three peaks around "mid-day," one shortly before "mid-day," a second at circadian maximum (i.e., for maximal R), and the third shortly after mid-day. These peaks reflect variations in activity and synaptic signaling as R(t) and G(t) values traverse the DLAMO region of the  $F(G, R, E_{GABA})$  surfaces. Increasing  $g_0$  from weak coupling reduces and eventually eliminates the second peak at "mid-day," resulting in a "mid-day" dip in firing rates.

Variability in the level of high SCN neural activity, including dips, has been observed in recordings of SCN neural firing activity particularly under long photoperiods [41, 50]. While the significance of such mid-day dips in SCN firing rates is unclear, we speculate that they could contribute to the well-documented increased tendency to sleep in afternoons [7] and the afternoon dip in alertness [33] in humans.

Other phenomena predicted by our model are that the standard deviations of firing rates are highly variable, varying in patterns similar to the variations in firing rates but often surging at circadian "sunrise" and "sunset." Tracking trajectories of total synaptic conductances show that these surges occur when neural firing states approach and cross boundaries between firing regimes—where sunrise corresponds to the transition from rest to AP firing, and sunset corresponds to the transition from AP firing to rest. Recordings of individual SCN neural activity show high variance, particularly in the dorsal region, with some units reaching peak firing at the transition when lights turn on or off, in contrast to the majority of units firing during lights on [8]. The high firing-rate variance at these transitions suggests that SCN signaling may become more incoherent and perhaps contribute to "sundowning" [30], in which certain neuropsychiatric conditions become exacerbated in dementia patients, for example, at or around sunset. There is evidence that sundowning is mediated by degeneration of the SCN [30] and can be improved with bright light therapy which increases amplitude and reduces variance in SCN neural activity [3].

Outside of this surging tendency at boundaries between firing regimes, firing-rate standard deviations were strongly positively correlated with the total synaptic conductance G. Hence, increasing parameters which increased total synaptic conductance, such as maximum synaptic conductance  $g_0$ , tended to increase standard deviations of firing rates. Firing-rate standard deviations also increased as standard deviations in  $E_{GABA}$ , in circadian phases, and in  $N_{syn}$  increased. Notably, the increase in firing-rate standard deviation as  $Var(N_{syn})$  increased

appeared to be the only strong effect on network firing-rate statistics of changing the network connectivity structure, when average connection density  $\overline{N}_{sun}$  was held constant.

**5.3. SCN model limitations.** Despite the potential predictive power of our model, our results have several limitations. In particular, we have assumed that the mean circadian proxy R(t) varies sinusoidally throughout the day. As mentioned above, this assumption captures the observed oscillations in firing characteristics of SCN neurons [4, 5] and generates the observed oscillations in firing rates [8, 34, 35, 36, 50]. However, a more accurate time profile for R(t) may be determined by matching experimental data on the time course of daily changes in SCN firing properties with the effects of R on firing state in the SCN neuron model. Existing data provides information on SCN neural firing at different time points across the day, and current work is focused on estimating the appropriate continuous time profile to capture this data. Further work is needed, however, to understand how external light schedules may influence the course of SCN neuron firing patterns across the day.

Model results would also be improved by incorporating additional distributions of properties of SCN neurons. For example, variation in the period of the molecular circadian clocks across the SCN could be included. It may also be appropriate to incorporate spatial heterogeneity into our model. Indeed, as mentioned earlier in the Discussion, it may be appropriate to model the SCN as two populations—one population each for the dorsal (core) and ventral (shell) portions of the SCN. Not only may these regions play functionally different roles in the SCN [54], but important neuronal properties may differ between these regions. For instance,  $E_{GABA}$  is typically lower in the ventral than the dorsal SCN [16], and differences in circadian phases between the dorsal and ventral SCN have been reported [21].

Further, studies such as [1] indicate that ventral SCN neurons have more functional connections than do dorsal SCN neurons. This in turn suggests that neurons in the ventral SCN may share a larger number of synaptic connections with other SCN neurons than do dorsal SCN neurons. Due to the larger number of synapses, ventral SCN neurons would likely experience more synaptic signaling and thus higher total synaptic conductances G than dorsal SCN neurons. Because ventral SCN neurons, as mentioned above, also have lower values of  $E_{GABA}$ , there would be an anticorrelation between G and  $E_{GABA}$  in the SCN. Such anticorrelation would violate the assumption of independence we have made to calculate the probability distribution of  $(G, R, E_{GABA})$  across SCN neurons, potentially altering predicted mean firing rates.

Finally, even if such assumptions of independence are not violated, it is not clear what the distribution of the total synaptic conductance G, alone, should be at any particular time. Indeed, even though we have provided conditions that would make G normally distributed, such conditions require that  $Var(N_{syn})$  be much smaller than  $\overline{N_{syn}}$ , which is unknown. Nevertheless, the aforementioned functional connectivity study finds that functional connections in the SCN follow a power-law degree distribution [1], which, if also true of the synaptic connections, would help us better understand the distribution of G.

Also potentially affecting the distribution of G and SCN firing activity in general is the presence of gap junctions in the SCN. Indeed, it has been shown that gap junctions play a role, in particular, in synchronizing SCN neurons [51]. However, our model only takes into account chemical synapses in its current formulation and, as it only summarizes firing-rate statistics, is not able to directly account for synchrony between SCN neurons.

**5.4.** Conclusions. Despite the limitations, our mean-field firing-rate model for the SCN network makes predictions about the effects on population firing statistics of the unique properties of the SCN neural network, such as circadian phase effects on firing state, distributions of GABA reversal potentials, and modulation of synaptic signaling due to atypical neuron firing states. In doing so, our model clarifies how these properties can lead to circadian disruptions, such as the blunted circadian rhythm amplitude associated with aging and neurophysiological diseases. More generally, our model formalism provides a new method to capture the effects of heterogeneity in the electrophysiological properties across neurons on the network firing-rate statistics.

Appendix A. Parameters for the application to the SCN. In Table 2 below, we summarize the abbreviations, default values, valid range, and default units for parameters used to apply the model specifically to the SCN. Note that some parameters have parameter ranges outside of which our model does not function. Namely,  $R_{ampl}$ ,  $\overline{E_{GABA}}$ , and  $\sigma_{EGABA}$  are restricted by the values of R and  $E_{GABA}$  over which we have calculated  $Y(G, R, E_{GABA})$  and  $F(G, R, E_{GABA})$ . On the other hand,  $\sigma_{\theta}$ , and  $g_0$  make the model impractically slow or subject to noise if they exceed the parameter range.

Table 2

Summary of parameters for the application to the SCN: In the table, [a], [b], [c], [d] indicate that respective values are due to [1], [39], [16], and [55]. [e] Indicates that in particular, we need that  $\sigma_{EGABA} \leq$  $\frac{1}{5} \max(|\overline{E_{GABA}} + 110)|, |\overline{E_{GABA}}|)$ , or else when integrating over the  $E_{GABA}$  distribution when calculating expectations of firing rates, we exceed the valid parameter range. The maximum value of  $\sigma_{EGABA}$  therefore is 11 mV, occurring when  $\overline{E_{GABA}} = -55 \ mV$ .

Parameter	Abbreviation	Default	Range	Units
Number of neurons in	N	$10,000^{[a]}$	-	Number of neurons
simulation				
Average number of	$\overline{N_{syn}}$	$1{,}100^{[b]}$	-	Number of synapses
synapses into a neuron				
Variance in the number	$Var(N_{syn})$	979	$0-(N-\overline{N_{syn}})\overline{N_{syn}}$	Number of synapses
of synapses into neurons		D (0(1))		27/4
Circadian proxy	R	$R_{ampl} \sin(\theta(t))$	-8.5 - 8.5	N/A
Circadian proxy	$R_{ampl}$	$5^{[c]}$	0 - 8.5	N/A
amplitude	_			
Mean circadian phase	$\overline{ heta}$	Time dependent	$0-2\pi$	Radians
Standard deviation in	$\sigma_{ heta}$	0.1	$0 \sim 3$	Radians
circadian phase		[1.1		
Mean GABA reversal	$E_{GABA}$	$-55^{[b]}$	-110 - 0	$\mathrm{mV}$
potential		ru-1	[-]	
Standard deviation in	$\sigma E_{GABA}$	$7^{[\mathrm{b}]}$	$0 - 11^{[e]}$	$\mathrm{mV}$
$E_{GABA}$		4	2	
Maximum synaptic conductance	g <sub>0</sub>	$5 \cdot 10^{-4}$	$0 - \approx 10^{-2}$	$nS/cm^2$
Synaptic time constant	au	$34^{[d]}$	-	ms

**Appendix B. Numerical simulations.** All simulations were conducted using MATLAB, and code is available upon request to the authors.

The convolutions used to find the statistics for synaptic conductance, g, rewritten as differential equations, were solved using an Euler-step algorithm. Notably, switching to more stable algorithms such as Runge–Kutta in no cases significantly improved the smoothness of solutions. Further, at times the step-size for the Euler-step algorithm had to be reduced to increase the smoothness of solutions.

The data underlying the F-G-R- $E_{GABA}$ , Y-G-R- $E_{GABA}$ , and YF-G-R- $E_{GABA}$  surfaces was generated by solving the Hodgkin–Huxley type differential equations of Diekman [17] over about 2 seconds for roughly 6,000,000 combinations of G, R, and  $E_{GABA}$  values. To do so we took advantage MATLAB's parallel computing capabilities by running the code on the Great Lakes Computing Cluster using 12 cores over the course of about 20 hours.

To extrapolate from this data to the continuous functions  $F(G, R, E_{GABA})$  and  $Y(G, R, E_{GABA})$ , we linearly interpolated piecewise between data points. However, to reduce numerical noise introduced by integrating over piecewise linear interpolations of the original data in simulations for model results, polynomial fits of  $F(G, R, E_{GABA})$  and  $YF(G, R, E_{GABA})$  data, as well as of the corresponding boundaries between firing regimes, were computed for each firing regime present when  $E_{GABA} = -55$  mV. In simulations of our firing-rate model where  $E_{GABA} = -55$  mV for all neurons in the network, these fits were used instead of the linear interpolations of the data. In particular, the polynomial fits can be seen in the figures displaying model simulations where  $\sigma_{EGABA} = 0$  and  $\overline{E_{GABA}} = -55$  mV (Figures 5–7, and the second column of Figure 11). Fits for each firing regime seen in F(G, R, -55) and YF(G, R, -55) as well as for the corresponding boundaries were made using MATLAB's "fit" command, using a mixture of built-in and custom fit-types.

Finally, to calculate the integrals for standard deviations and means of firing rates f and yf, we used trapezoidal integration modified to take into account the sparsity of and to interpolate over the F-G-R- $E_{GABA}$  and YF-G-R- $E_{GABA}$  surfaces. To further increase the speed of our algorithm, we only integrated within five standard deviations of the center of the distributions for G, R, and  $E_{GABA}$ , as the contributions of the integrand from other values of G, R, and  $E_{GABA}$  were negligibly small in our simulations.

Appendix C. Characteristic function for total synaptic conductance. The characteristic function for total synaptic conductance G may be used to specify the shape of the G distribution and is a function of the statistics for  $N_{syn}$  and g. In particular, if we strengthen our assumptions that  $g_{j,i}(t)$  for  $j = 1, ..., N_{syn,i}$  are pairwise uncorrelated with one another and are independent of  $N_{syn,i}$  by instead assuming that  $g_{j,i}(t)$  for  $j = 1, ..., N_{syn,i}$  and  $N_{syn,i}$  form a mutually independent collection of random variables, we have that the characteristic function is

$$\phi_{G}(x) = \mathbb{E}\left[e^{ixG(t)}\right]$$

$$= \mathbb{E}\left[e^{ix\sum_{j=1}^{N_{syn_{i}}}g_{j,i}}\right]$$

$$= \mathbb{E}\left[\Pi_{j=1}^{N_{syn_{i}}}e^{ixg_{j,i}}\right]$$

$$= \mathbb{E}\left[\mathbb{E}\left[\Pi_{j=1}^{N_{syn_{i}}}e^{ixg_{j,i}}|N_{syn,i}\right]\right]$$

$$\begin{split} &= \mathbb{E}\left[\Pi_{j=1}^{N_{syn_i}} \mathbb{E}\left[e^{ixg_{j,i}}|N_{syn,i}\right]\right] \\ &= \mathbb{E}\left[\Pi_{j=1}^{N_{syn_i}} \mathbb{E}\left[e^{ixg}\right]\right] \\ &= \mathbb{E}\left[\left(\phi_g(x)\right)^{N_{syn}}\right], \end{split}$$

and hence

$$\phi_G = \mathcal{G}_{N_{syn}}(\phi_g),$$

where  $\mathcal{G}_{N_{syn}}$ , the probability generating function of  $N_{syn}$ , is determined exclusively by the degree distribution of the network.

Appendix D. Single-cell SCN neuron model. Diekman's single-cell SCN neuron model [17] states that the membrane voltage V of an SCN neuron is modeled by

$$C\frac{dV}{dt} = I_{app} - I_{Na} - I_K - I_{CaL} - I_{CaNonL} - I_{KCa}(R) - I_{K-leak}(R) - I_{Na-leak},$$

where C = 5.7 pF, voltage is in mV, and membrane currents  $I_x$  in pA are given in Table 3.

The gating variables  $q = m, h, n, r_L, r_{NonL}, f_{NonL}$  follow

$$\frac{dq}{dt} = \frac{q_{\infty}(V(t)) - q(t)}{\tau_q(V(t))},$$

the gating variable s follows

$$\frac{ds}{dt} = \frac{s_{\infty}(Ca_s(t)) - s(t)}{\tau_q(Ca_s(t))},$$

 $f_L$  follows

$$f_L = \frac{K_1}{K_2 + Ca_s(t)},$$

Table 3

Formulas (2nd column) for ionic currents (1st column) and corresponding constants (3rd and 4th columns) as appearing in the single neuron model of [17].

Current (pA)	Formula	Max conductance (nS)	Reversal potential (mV)
$I_{Na}$	$g_{Na}m^3(t)h(t)\cdot(V(t)-E_{Na})$	$g_{Na} = 229$	$E_{Na} = 45$
$I_K$	$g_K n^4(t) \cdot (V(t) - E_K)$	$g_K = 3$	$E_K = -97$
$I_{CaL}$	$g_{CaL}r_L(t)f_L(Ca_s(t))\cdot(V(t)-E_{Ca})$	$g_{CaL} = 6$	$E_{Ca} = 54$
$I_{CaNonL}$	$g_{CaNonL}r_{NonL}(t)f_{NonL}(t)\cdot(V(t)-E_{Ca})$	$g_{CaNonL} = 20$	$E_{Ca} = 54$
$I_{KCa}(R)$	$g_{KCa}(R)s^2(t)\cdot(V(t)-E_K)$	$g_{KCa} = \frac{198}{1 + exp(R) + 2}$	$E_K = -97$
$I_{K-leak}(R)$	$g_{K-leak}(R) \cdot (V(t) - E_K)$	$g_{KCa} = \frac{198}{1 + exp(R) + 2}$ $g_{K-leak} = \frac{0.2}{1 + exp(R)}$	$E_K = -97$
$I_{Na-leak}$	$g_{Na-leak} \cdot (V(t) - E_{Na})$	$g_{Na-leak} = 0.0576$	$E_{Na} = 45$

Table 4

The gating variables (2nd column) involved in the dynamics of each type of ionic current (1st column). The 3rd and 4th columns describe the activation functions and the time constants for each gating variable.

Current type (pA)	Gating variable $q$	$q_{\infty}$	$ au_q$
$I_{Na}$	m	$\frac{1}{1 + exp(-(V(t) + 35.2)/8.1)}$	$\exp(-(V(t) + 286)/160)$
$I_{Na}$	h	$\frac{1}{1 + exp((V(t) + 62)/2)}$	$0.51 + \exp(-(V(t) + 26.6)/7.1)$
$I_K$	n	$\frac{1}{[1+exp(-(V_{(t)}-14)/17)]^{0.25}}$	$\exp(-(V(t) - 67)/68)$
$I_{CaL}$	$r_L$	$\frac{1}{1+exp(-(V(t_1)+36)/5.1)}$	3.1
$I_{CaNonL}$	$r_{NonL}$	$\frac{1}{1+exp(-(V(t)+21.6)/6.7)}$	3.1
$I_{CaNonL}$	$f_{NonL}$	1	$\exp(-(V(t) - 444)/220)$
$I_{KCa(R)}$	s	$\frac{1+exp((V(t)+260)/65)}{10^7(Ca_s)^2}$ $\frac{10^7(Ca_s)^2}{10^7(Ca_s)^2+5.6}$	$\frac{500}{10^7 (Ca_s)^2 + 5.6}$

where  $K_1 = 3.93E - 5$ mM,  $K_2 = 6.55E - 4$ mM, and  $Ca_s$  follows

$$\frac{dCa_s}{dt} = -k_s(I_{CaL}(t) + I_{CaNonL}(t)) - Ca_s/\tau_s + b_s,$$

where  $k_s = 1.65E - 4$  mM/fC and  $b_s = 5.425E - 4$  mM/ms. Steady state activation functions  $q_{\infty}$  and time constants  $\tau_q$  for the gating variables are given in Table 4.

**Appendix E. Verification of differential equations.** We show that the convolutions from (2.14) and (2.15),

$$\overline{g}(t) = \overline{H \star yf} = (H \star \overline{yf})(t) = \int_0^t H(t-s)\overline{yf}(s)ds,$$

$$\sigma_g(t) = (H \star \sigma_{yf})(t) = \int_0^t H(t-s)\sigma_{yf}(s)ds,$$

may be written as the differential equations from (2.16) and (2.17),

$$\overline{g}'' = -2\tau^{-1}\overline{g}' - \tau^{-2}\overline{g} + e\tau^{-1}g_0\overline{yf}(t),$$
  
$$\sigma_g'' = -2\tau^{-1}\sigma_g' - \tau^{-2}\sigma_g + e\tau^{-1}g_0\sigma_{yf}(t).$$

To verify these equations, observe that

$$\begin{split} \frac{d}{dt} \left[ \int_0^t H(t-s)\overline{yf}(s)ds \right] &= \frac{d}{dt} \left[ \int_0^t e \cdot g_0 \frac{t-s}{\tau} e^{-(t-s)/\tau} \overline{yf}(s)ds \right] \\ &= \frac{g_0 e}{\tau} \frac{d}{dt} \left[ e^{-t/\tau} t \int_0^t e^{s/\tau} \overline{yf}(s)ds - e^{-t/\tau} \int_0^t s e^{s/\tau} \overline{yf}(s)ds \right] \\ &= \frac{g_0 e}{\tau} \left[ e^{-t/\tau} \left( 1 - \frac{t}{\tau} \right) \int_0^t e^{s/\tau} \overline{yf}(s)ds + t \overline{yf}(t) - \left( -e^{-t/\tau} \int_0^t \frac{s}{\tau} e^{s/\tau} \overline{yf}(s)ds + t \overline{yf}(t) \right) \right] \end{split}$$

$$\begin{split} &=\frac{g_0e}{\tau}\left[e^{-t/\tau}\left(1-\frac{t}{\tau}\right)\int_0^t e^{s/\tau}\overline{yf}(s)ds+\frac{1}{\tau}e^{-t/\tau}\int_0^t se^{s/\tau}\overline{yf}(s)ds\right]\\ &=e^{-t/\tau}\frac{g_0e}{\tau}\left[\left(1-\frac{t}{\tau}\right)\int_0^t e^{s/\tau}\overline{yf}(s)ds+\frac{1}{\tau}\int_0^t se^{s/\tau}\overline{yf}(s)ds\right]\\ &=\frac{g_0e}{\tau}\int_0^t \left(1-\frac{t}{\tau}+\frac{s}{\tau}\right)e^{-(t-s)/\tau}\overline{yf}(s)ds \end{split}$$

and

$$\begin{split} &\frac{d^2}{dt^2}\left[\int_0^t H(t-s)\overline{yf}(s)ds\right] \\ &= \frac{g_0e}{\tau}\left(\frac{e^{-\frac{t}{\tau}}}{-\tau}\left[\left(1-\frac{t}{\tau}\right)\int_0^t e^{\frac{s}{\tau}}\overline{yf}(s)ds + \frac{1}{\tau}\int_0^t se^{\frac{s}{\tau}}\overline{yf}(s)ds\right] \\ &+ e^{-\frac{t}{\tau}}\left[\frac{d}{dt}\left(\left(1-\frac{t}{\tau}\right)\int_0^t e^{\frac{s}{\tau}}\overline{yf}(s)ds\right) + \frac{t}{\tau}e^{\frac{t}{\tau}}\overline{yf}(t)\right]\right) \\ &= e^{-\frac{t}{\tau}}\frac{g_0e}{\tau}\left[\left(\frac{t}{\tau^2} - \frac{1}{\tau}\right)\int_0^t e^{\frac{s}{\tau}}\overline{yf}(s)ds - \frac{1}{\tau^2}\int_0^t se^{\frac{s}{\tau}}\overline{yf}(s)ds - \frac{1}{\tau}\int_0^t e^{\frac{s}{\tau}}\overline{yf}(s)ds + \left(1-\frac{t}{\tau}\right)e^{\frac{t}{\tau}}\overline{yf}(t) + \frac{t}{\tau}e^{\frac{t}{\tau}}\overline{yf}(t)\right] \\ &= e^{-t/\tau}\frac{g_0e}{\tau}\left[\left(\frac{t}{\tau^2} - \frac{2}{\tau}\right)\int_0^t e^{s/\tau}\overline{yf}(s)ds - \frac{1}{\tau^2}\int_0^t se^{s/\tau}\overline{yf}(s)ds + e^{t/\tau}\overline{yf}(t)\right] \\ &= e^{-t/\tau}\frac{g_0e}{\tau}\left[\left(\frac{t}{\tau^2} - \frac{2}{\tau}\right)\int_0^t e^{s/\tau}\overline{yf}(s)ds - \frac{1}{\tau^2}\int_0^t se^{s/\tau}\overline{yf}(s)ds\right] + \frac{g_0e}{\tau}\overline{yf}(t) \\ &= e^{-t/\tau}\frac{g_0e}{\tau}\left[\left(\frac{t}{\tau^2} - \frac{2}{\tau}\right)\int_0^t e^{s/\tau}\overline{yf}(s)ds - \frac{1}{\tau^2}\int_0^t se^{s/\tau}\overline{yf}(s)ds\right] + \frac{g_0e}{\tau}\overline{yf}(t) \\ &= -e^{-t/\tau}\frac{g_0e}{\tau^2}\left[\left(2-\frac{t}{\tau}\right)\int_0^t e^{s/\tau}\overline{yf}(s)ds + \frac{1}{\tau}\int_0^t se^{s/\tau}\overline{yf}(s)ds\right] + \frac{g_0e}{\tau}\overline{yf}(t) \\ &= -\frac{g_0e}{\tau^2}\int_0^t \left(2-\frac{t}{\tau} + \frac{s}{\tau}\right)e^{-(t-s)/\tau}\overline{yf}(s)ds + \frac{g_0e}{\tau}\overline{yf}(t), \end{split}$$

and thus

$$\begin{split} \frac{d^2}{dt^2} \left[ \int_0^t H(t-s)\overline{yf}(s)ds \right] + \frac{2}{\tau} \frac{d}{dt} \left[ \int_0^t H(t-s)\overline{yf}(s)ds \right] + \frac{1}{\tau^2} \int_0^t H(t-s)\overline{yf}(s)ds - \frac{g_0e}{\tau} \overline{yf}(t) \\ &= \frac{g_0e}{\tau^2} \int_0^t \left[ -\left(2 - \frac{t}{\tau} + \frac{s}{\tau}\right) + 2\left(1 - \frac{t}{\tau} + \frac{s}{\tau}\right) + \left(\frac{t-s}{\tau}\right) \right] e^{-(t-s)/\tau} \overline{yf}(s)ds \\ &= 0. \end{split}$$

as desired. An analogous argument shows that (2.15) may be rewritten as (2.17).

Appendix F. Validating model results against a spiking neuronal network. To validate the predictions of our firing-rate model, we simulated a network of biophysical model SCN neurons. The 100-cell network has connectivity similar to the networks underlying results shown in Figures 5–10. In particular, synaptic structure is based on a Poisson random graph with 11% connectivity. The dynamics of each neuron is modeled using the Hodgkin–Huxley-type SCN neuron model from (3.2), and GABAergic synaptic gating was modeled with (3.4). Total synaptic conductance G(t) for each neuron is computed by linearly summing synaptic gating variables over all presynaptic neurons and multiplying by a maximum synaptic conductance  $g_0$ . The value of  $g_0$  is chosen to be  $0.5/\overline{N_{syn}}$  nS/cm<sup>2</sup>, similar to the value used in the firing-rate model. This results in values of G(t) between 0 and roughly 0.5 nS/cm<sup>2</sup>. Synaptic current in each postsynaptic cell is modeled by (3.3) where V(t) is the membrane potential of the postsynaptic cell.

To validate the ability of the firing-rate model to capture the effects of heterogeneities in the spiking network model, we simulate the spiking network model for two combinations

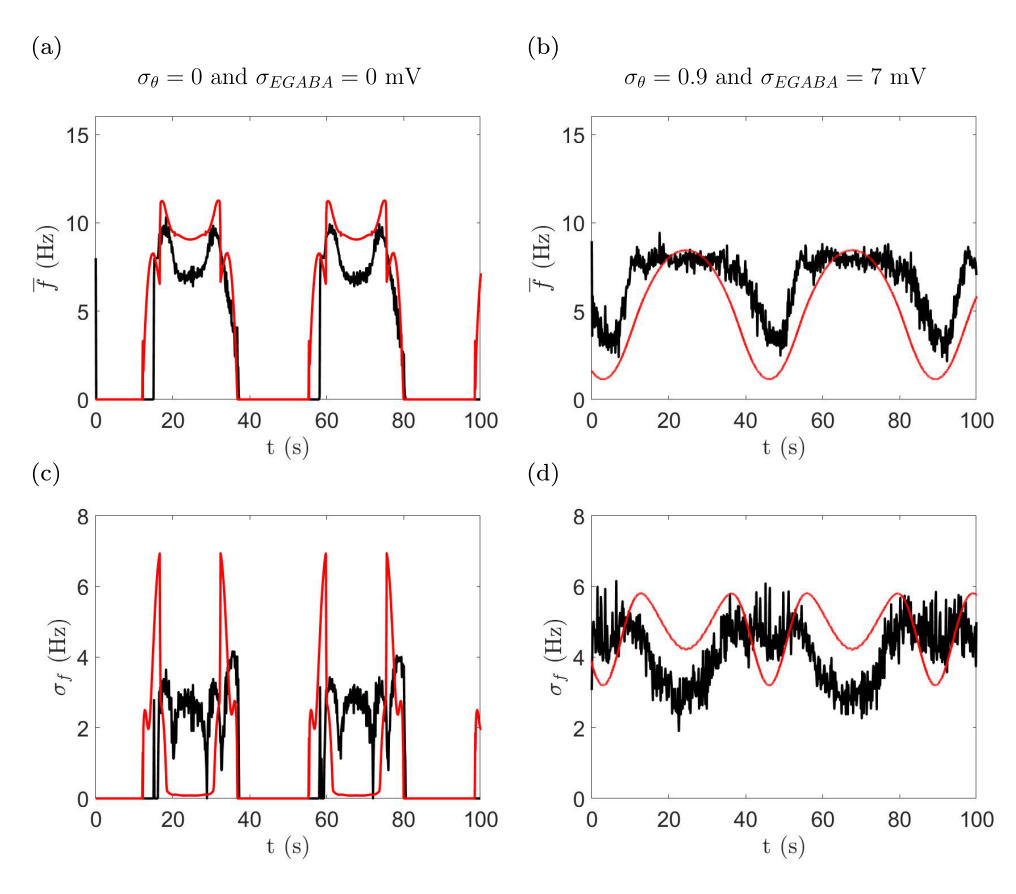


Figure 10. Comparison of firing-rate model results to activity in a spiking neuronal network. Mean firing rates (top row) and standard deviations (bottom row) for the firing-rate model (red curves) and for a network of 100 SCN model neurons (black curves). (a,c) No variance in circadian phases or  $E_{GABA}$  ( $\sigma_{\theta} = 0$  and  $\sigma_{EGABA} = 0$  mV). (b,d)  $\sigma_{\theta} = 0.9$  and  $\sigma_{EGABA} = 7$  mV as in Figure 9. In the firing-rate model,  $g_0 = 5 \cdot 10^{-4}$  nS/cm<sup>2</sup>,  $R_{ampl} = 5$ ,  $\overline{N_{syn}} = 1,100$  and  $Var(N_{syn}) = 979$ .

of standard deviations in circadian phase values,  $\sigma_{\theta}$ , and in GABA reversal potential values,  $\sigma_{EGABA}$ . Specifically, we simulate a network with no variance in circadian phases or  $E_{GABA}$  ( $\sigma_{\theta} = 0$  and  $\sigma_{EGABA} = 0$  mV) and a network where the variances were set to their largest values considered in Figure 9 ( $\sigma_{\theta} = 0.9$  and  $\sigma_{EGABA} = 7$  mV). In both these networks, mean  $E_{GABA}$  was set to -55 mV, the amplitude  $R_{ampl}$  of the circadian proxy was 5, and in the latter network both  $E_{GABA}$  and circadian phase followed Gaussian distributions.

To compare the firing-rate statistics of the firing-rate model to the average activity of the spiking network, we calculate the mean  $\overline{f}$  and standard deviations  $\sigma_f$  of the firing rates across the spiking network. To do so, we bin the spiking activity into 0.125 seconds intervals, count the number of spikes for each neuron in each bin, and divide the spike counts by the bin width to arrive at time-varying, mean firing rates for each neuron. We then compute the mean and standard deviations of cellular firing rates across all neurons during each bin.

As shown in Figure 10, the firing-rate statistics of the spiking network qualitatively reproduce the predictions of our firing-rate model. In particular, the peaks and troughs of  $\overline{f}$  and  $\sigma_f$  predicted by the spiking network occur roughly at the same time as those predicted by our firing-rate model. Moreover, each model's predictions of  $\overline{f}$  typically differ by only up to a few hertz for both the simulation with  $\sigma_{\theta} = 0$  and  $\sigma_{EGABA} = 0$  mV and the simulation with  $\sigma_{\theta} = 0.9$  and  $\sigma_{EGABA} = 7$  mV. However, while both models' predictions of  $\sigma_f$  have similar magnitudes, it should be noted that since the spiking network is small and the simulation time is relatively short (lasting 100 seconds), the magnitudes of  $\sigma_f$  predicted by the spiking network increase with decreasing bin width. Consequently, comparisons between  $\sigma_f$  output by the two types of models are best made qualitatively.

Appendix G. Effect of changing  $E_{GABA}$ . The effects of  $E_{GABA}$  on network synaptic conductance and firing rates are shown in Figure 11 where three different values of  $E_{GABA}$  are considered: -80 mV, -55 mV, and -32 mV. To isolate the effects of changing  $E_{GABA}$ , we assume there to be no variance in circadian phase  $\sigma_{\theta} = 0$  or in  $E_{GABA}$  itself ( $\sigma_{EGABA} = 0$ ). We find that higher values of  $E_{GABA}$  lead to higher firing rates, with a "mid-day" dip occurring for the largest  $R_{ampl}$  (left column) when maximum synaptic conductance is at a moderate level ( $g_0 = 5 \cdot 10^{-4} \text{ mS/cm}^2$ ). For lower  $R_{ampl}$ , the mid-day dip is flattened out since network activity doesn't reach the DLAMO region (middle column), and for smallest  $R_{ampl}$ , firing rate varies approximately sinusoidally. Firing-rate standard deviations (middle row) remain small, except for brief spikes as network activity transitions between AP firing and subthreshold regimes.

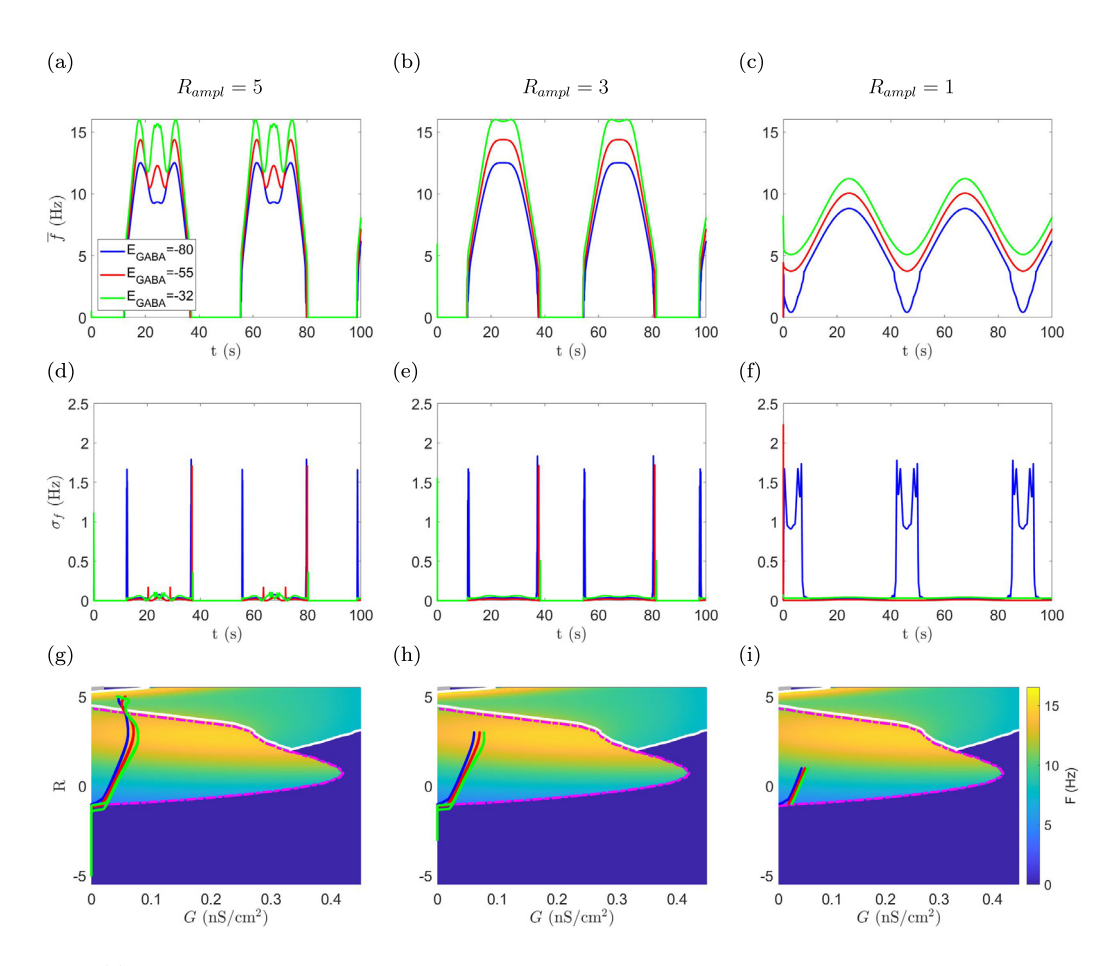


Figure 11. Effect of  $E_{GABA}$  on firing rates when variance in  $E_{GABA}$  and circadian phase are not present and synaptic coupling is weak, fixed at  $g_0 = 5 \cdot 10^{-5}$  for all neurons. (a–f) Mean firing rates f(t) (first row) and standard deviations of firing rates  $\sigma_f(t)$  (2nd row) over multiple R(t) cycles (shortened circadian cycles) for 3 different values of GABA reversal potential  $E_{GABA}$  (in mV), -55 mV likely being the mean  $E_{GABA}$  in the SCN. Three amplitudes of circadian variation are simulated,  $R_{ampl} = 5$  (left column), 3 (middle column), and 1 (right column). (g–i) Trajectories (G(t), R(t)) are plotted on the neuronal firing rate surface F(G, R, -55) for the same values of  $E_{GABA}$  as in (a–f). Firing-rate standard deviations tend to be largest near transitions between firing regimes.

**Acknowledgment.** The authors would like to thank Cecilia Diniz-Behn, Michal Zochowski, and Danny Forger for their input and suggestions on this project.

## REFERENCES

- [1] J. H. ABEL, K. MEEKER, D. GRANADOS-FUENTES, P. C. S. JOHN, T. J. WANG, B. B. BALES, F. J. DOYLE, E. D. HERZOG, AND L. R. PETZOLD, Functional network inference of the suprachiasmatic nucleus, Proc. Natl. Acad. Sci. USA, 113 (2016), pp. 4512–4517, https://doi.org/10.1073/pnas.1521178113.
- [2] S.-I. Amari, Dynamics of pattern formation in lateral-inhibition type neural fields, Biol. Cybern., 27 (1977), pp. 77–87, https://doi.org/10.1007/BF00337259.
- [3] B. BANO-OTALORA, F. MARTIAL, C. HARDING, D. A. BECHTOLD, A. E. ALLEN, T. M. BROWN, M. D. BELLE, AND R. J. Lucas, Bright daytime light enhances circadian amplitude in a diurnal mammal, Proc. Natl. Acad. Sci. USA, 118 (2021), e2100094118, https://doi.org/10.1073/pnas.2100094118.
- [4] B. BANO-OTALORA, M. J. MOYE, T. BROWN, R. J. LUCAS, C. O. DIEKMAN, AND M. D. BELLE, Daily electrical activity in the master circadian clock of a diurnal mammal, eLife, 10 (2021), e68179, https://doi.org/10.7554/eLife.68179.
- [5] M. D. Belle, C. O. Diekman, D. B. Forger, and H. D. Piggins, Daily electrical silencing in the mammalian circadian clock, Science, 326 (2009), pp. 281–284, https://doi.org/10.1126/science.1169657.
- [6] P. C. Bressloff, Stochastic neural field model of stimulus-dependent variability in cortical neurons, PLoS Comput. Biol., 15 (2019), e1006755, https://doi.org/10.1371/journal.pcbi.1006755.
- [7] R. J. BROUGHTON AND D. F. DINGES, Sleep and Alertness: Chronobiological, Behavioral, and Medical Aspects of Napping, Raven Press, New York, 1989.
- [8] T. Brown and H. Piggins, Spatiotemporal heterogeneity in the electrical activity of suprachiasmatic nuclei neurons and their response to photoperiod, J. Biol. Rhythms, 24 (2009), pp. 44–54, https://doi.org/10.1177/0748730408327918.
- [9] G. BUZSÁKI AND K. MIZUSEKI, The log-dynamic brain: How skewed distributions affect network operations, Nat. Rev. Neurosci., 15 (2014), pp. 264–278, https://doi.org/10.1038/nrn3687.
- [10] Á. BYRNE, R. D. O'DEA, M. FORRESTER, J. ROSS, AND S. COOMBES, Next-generation neural mass and field modeling, J. Neurophysiol., 123 (2020), pp. 726–742, https://doi.org/10.1152/jn.00406.2019.
- [11] M. CARLU, O. CHEHAB, L. DALLA PORTA, D. DEPANNEMAECKER, C. HÉRICÉ, M. JEDYNAK, E. KÖKSAL ERSÖZ, P. MURATORE, S. SOUIHEL, C. CAPONE, Y. ZERLAUT, A. DESTEXHE, M. DI VOLO, A mean-field approach to the dynamics of networks of complex neurons, from non-linear integrate-and-fire to Hodgkin-Huxley models, J. Neurophysiol., 123 (2020), pp. 1042–1051, https://doi.org/10.1152/jn.00399.2019.
- [12] A. V. CHIZHOV AND L. J. GRAHAM, Population model of hippocampal pyramidal neurons, linking a refractory density approach to conductance-based neurons, Phys. Rev. E, 75 (2007), 011924, https://doi.org/10.1103/PhysRevE.75.011924.
- [13] A. N. Coogan, B. Schutová, S. Husung, K. Furczyk, B. T. Baune, P. Kropp, F. Hässler, and J. Thome, The circadian system in Alzheimer's disease: Disturbances, mechanisms, and opportunities, Biol. Psychiatry, 74 (2013), pp. 333–339, https://doi.org/10.1016/j.biopsych.2012.11.021.
- [14] F. L. DA SILVA, A. HOEKS, H. SMITS, AND L. ZETTERBERG, Model of brain rhythmic activity, Kybernetik, 15 (1974), pp. 27–37, https://doi.org/10.1007/BF00270757.
- [15] G. DECO, V. K. JIRSA, P. A. ROBINSON, M. BREAKSPEAR, AND K. FRISTON, The dynamic brain: From spiking neurons to neural masses and cortical fields, PLoS Comput. Biol., 4 (2008), e1000092, https://doi.org/10.1371/journal.pcbi.1000092.
- [16] D. DEWOSKIN, J. MYUNG, M. D. C. BELLE, H. D. PIGGINS, T. TAKUMI, AND D. B. FORGER, Distinct roles for gaba across multiple timescales in mammalian circadian timekeeping, Proc. Natl. Acad. Sci. USA, 112 (2015), pp. E3911–E3919, https://doi.org/10.1073/pnas.1420753112.
- [17] C. O. DIEKMAN, M. D. C. BELLE, R. P. IRWIN, C. N. ALLEN, H. D. PIGGINS, AND D. B. FORGER, Causes and consequences of hyperexcitation in central clock neurons, PLoS Comput. Biol., 9 (2013), pp. 1–11, https://doi.org/10.1371/journal.pcbi.1003196.
- [18] C. G. DINIZ BEHN AND V. BOOTH, Simulating microinjection experiments in a novel model

- of the rat sleep-wake regulatory network, J. Neurophysiol., 103 (2010), pp. 1937–1953, https://doi.org/10.1152/jn.00795.2009.
- [19] S. EL BOUSTANI AND A. DESTEXHE, A master equation formalism for macroscopic modeling of asynchronous irregular activity states, Neural. Comput., 21 (2009), pp. 46–100, https://doi.org/10.1162/neco.2009.02-08-710.
- [20] G. B. ERMENTROUT AND D. H. TERMAN, Mathematical Foundations of Neuroscience, Vol. 35, Springer Science & Business Media, New York, 2010.
- [21] J. A. Evans, T. L. Leise, O. Castanon-Cervantes, and A. J. Davidson, Dynamic interactions mediated by nonredundant signaling mechanisms couple circadian clock neurons, Neuron, 80 (2013), pp. 973–983, https://doi.org/10.1016/j.neuron.2013.08.022.
- [22] S. FARAJNIA, T. DEBOER, J. H. ROHLING, J. H. MEIJER, AND S. MICHEL, Aging of the suprachiasmatic clock, Neuroscientist, 20 (2014), pp. 44–55, https://doi.org/10.1177/1073858413498936.
- [23] S. Farajnia, S. Michel, T. Deboer, H. Tjebbe vanderleest, T. Houben, J. H. Rohling, A. Ramkisoensing, R. Yasenkov, and J. H. Meijer, *Evidence for neuronal desynchrony in the aged suprachiasmatic nucleus clock*, J. Neurosci., 32 (2012), pp. 5891–5899, https://doi.org/10.1523/JNEUROSCI.0469-12.2012.
- [24] G. B. FOLLAND, Real Analysis: Modern Techniques and Their Applications, Vol. 40, John Wiley & Sons, New York, 1999.
- [25] F.-H. GÜLDNER, Synaptology of the rat suprachiasmatic nucleus, Cell Tissue Res., 165 (1976), pp. 509–544, https://doi.org/10.1007/BF00224478.
- [26] M. H. HASTINGS, E. S. MAYWOOD, AND M. BRANCACCIO, Generation of circadian rhythms in the suprachiasmatic nucleus, Nat. Rev. Neurosci., 19 (2018), pp. 453–469, https://doi.org/10.1038/s41583-018-0026-z.
- [27] T. Heiberg, B. Kriener, T. Tetzlaff, G. T. Einevoll, and H. E. Plesser, Firing-rate models for neurons with a broad repertoire of spiking behaviors, J. Comput. Neurosci., 45 (2018), pp. 103–132, https://doi.org/10.1007/s10827-018-0693-9.
- [28] S. HOOD AND S. AMIR, The aging clock: Circadian rhythms and later life, J. Clin. Invest., 127 (2017), pp. 437–446, https://doi.org/10.1172/JCI90328.
- [29] Z. G. JIANG, Y. YANG, Z. P. LIU, AND C. N. ALLEN, Membrane properties and synaptic inputs of suprachiasmatic nucleus neurons in rat brain slices, J. Physiol., 499 (1997), pp. 141–159, https://doi.org/10.1113/jphysiol.1997.sp021917.
- [30] N. KHACHIYANTS, D. TRINKLE, S. J. SON, AND K. Y. KIM, Sundown syndrome in persons with dementia: An update, Psychiatry. Investig., 8 (2011), pp. 275, https://doi.org/10.4306/pi.2011.8.4.275.
- [31] Y. Leng, E. S. Musiek, K. Hu, F. P. Cappuccio, and K. Yaffe, Association between circadian rhythms and neurodegenerative diseases, Lancet Neurol., 18 (2019), pp. 307–318, https://doi.org/10.1016/S1474-4422(18)30461-7.
- [32] J. LESAUTER AND R. SILVER, Output signals of the SCN, Chronobiol Int., 15 (1998), pp. 535–550, https://doi.org/10.3109/07420529808998706.
- [33] V. Mavjee and J. Home, Boredom effects on sleepiness/alertness in the early afternoon vs. early evening and interactions with warm ambient temperature, Br. J. Psychol., 85 (1994), pp. 317–333, https://doi.org/10.1111/j.2044-8295.1994.tb02527.x.
- [34] J. Meijer, J. Schaap, K. Watanabe, and H. Albus, Multiunit activity recordings in the suprachiasmatic nuclei: In vivo versus in vitro models, Brain Res., 753 (1997), pp. 322–327, https://doi.org/10.1016/S0006-8993(97)00150-9.
- [35] J. H. Meijer, G. A. Groos, and B. Rusak, Luminance coding in a circadian pacemaker: The suprachiasmatic nucleus of the rat and the hamster, Brain Res., 382 (1986), pp. 109–118, https://doi.org/10.1016/0006-8993(86)90117-4.
- [36] J. H. Meijer, B. Rusak, and G. Gänshirt, The relation between light-induced discharge in the suprachiasmatic nucleus and phase shifts of hamster circadian rhythms, Brain Res., 598 (1992), pp. 257–263, https://doi.org/10.1016/0006-8993(92)90191-B.
- [37] M. MOLDAVAN, O. CRAVETCHI, AND C. N. ALLEN, Diurnal properties of tonic and synaptic GABA<sub>A</sub> receptor-mediated currents in suprachiasmatic nucleus neurons, J. Neurophysiol., 126 (2021), pp. 637–652, https://doi.org/10.1152/jn.00556.2020.
- [38] E. Montbrió, D. Pazó, and A. Roxin, Macroscopic description for networks of spiking neurons, Phys.

- Rev. X, 5 (2015), 021028, https://doi.org/10.1103/PhysRevX.5.021028.
- [39] R. Moore and M. E. Bernstein, Synaptogenesis in the rat suprachiasmatic nucleus demonstrated by electron microscopy and synapsin i immunoreactivity, J. Neurosci., 9 (1989), pp. 2151–2162, https://doi.org/10.1523/JNEUROSCI.09-06-02151.1989.
- [40] R. Y. Moore and J. C. Speh, GABA is the principal neurotransmitter of the circadian system, Neurosci. Lett., 150 (1993), pp. 112–116, https://doi.org/10.1016/0304-3940(93)90120-A.
- [41] M. MRUGALA, P. ZLOMANCZUK, A. JAGOTA, AND W. J. SCHWARTZ, Rhythmic multiunit neural activity in slices of hamster suprachiasmatic nucleus reflect prior photoperiod, Amer. J. Physiol. Regul. Integr. Compt. Physiol., 278 (2000), pp. R987–R994, https://doi.org/10.1152/ajpregu.2000.278.4.R987.
- [42] M. NAGANO, A. ADACHI, K.-I NAKAHAMA, T. NAKAMURA, M. TAMADA, E. MEYER-BERNSTEIN, A. SEHGAL, AND Y. SHIGEYOSHI, An abrupt shift in the day/night cycle causes desynchrony in the mammalian circadian center, J. Neurosci., 23 (2003), pp. 6141–6151, https://doi.org/10.1523/JNEUROSCI.23-14-06141.2003.
- [43] T. J. Nakamura, W. Nakamura, I. T. Tokuda, T. Ishikawa, T. Kudo, C. S. Colwell, and G. D. Block, Age-related changes in the circadian system unmasked by constant conditions, eNeuro, 2 (2015), ENEURO.0064-15.2015, https://doi.org/10.1523/ENEURO.0064-15.2015.
- [44] D. Q. NYKAMP AND D. TRANCHINA, A population density approach that facilitates large-scale modeling of neural networks: Analysis and an application to orientation tuning, J. Comput. Neurosci., 8 (2000), pp. 19–50, https://doi.org/10.1023/A:1008912914816.
- [45] J. R. PAUL, H. A. MUNIR, T. VAN GROEN, AND K. L. GAMBLE, Behavioral and scn neurophysiological disruption in the tg-swdi mouse model of Alzheimer's disease, Neurobiol. Dis., 114 (2018), pp. 194–200, https://doi.org/10.1016/j.nbd.2018.03.007.
- [46] C. M. PENNARTZ, M. T. DE JEU, N. P. Bos, J. SCHAAP, AND A. M. GEURTSEN, Diurnal modulation of pacemaker potentials and calcium current in the mammalian circadian clock, Nature, 416 (2002), pp. 286–290, https://doi.org/10.1038/nature728.
- [47] A. R. STINCHCOMBE, J. W. MOULAND, K. Y. WONG, R. J. LUCAS, AND D. B. FORGER, Multiplexing visual signals in the suprachiasmatic nuclei, Cell Rep., 21 (2017), pp. 1418–1425, https://doi.org/10.1016/j.celrep.2017.10.045.
- [48] J. Tabak, W. Senn, M. J. O'Donovan, and J. Rinzel, Modeling of spontaneous activity in developing spinal cord using activity-dependent depression in an excitatory network, J. Neurosci., 20 (2000), pp. 3041–3056, https://doi.org/10.1523/JNEUROSCI.20-08-03041.2000.
- [49] F. VAN OOSTERHOUT, E. A. LUCASSEN, T. HOUBEN, H. TJEBBE VANDERLEEST, M. C. ANTLE, AND J. H. MEIJER, Amplitude of the SCN clock enhanced by the behavioral activity rhythm, PLoS One, 7 (2012), e39693, https://doi.org/10.1371/journal.pone.0039693.
- [50] H. T. VANDERLEEST, T. HOUBEN, S. MICHEL, T. DEBOER, H. ALBUS, M. J. VANSTEENSEL, G. D. BLOCK, AND J. H. MEIJER, Seasonal encoding by the circadian pacemaker of the SCN, Curr. Biol., 17 (2007), pp. 468–473, https://doi.org/10.1016/j.cub.2007.01.048.
- [51] M.-H. Wang, N. Chen, and J.-H. Wang, The coupling features of electrical synapses modulate neuronal synchrony in hypothalamic superachiasmatic nucleus, Brain Res., 1550 (2014), pp. 9–17.
- [52] A. WATANABE, S. SHIBATA, AND S. WATANABE, Circadian rhythm of spontaneous neuronal activity in the suprachiasmatic nucleus of old hamster in vitro, Brain Res., 695 (1995), pp. 237–239, https://doi.org/10.1016/0006-8993(95)00713-Z.
- [53] H. R. WILSON AND J. D. COWAN, Excitatory and inhibitory interactions in localized populations of model neurons, Biophys. J., 12 (1972), pp. 1–24, https://doi.org/10.1016/S0006-3495(72)86068-5.
- [54] L. YAN, I. KARATSOREOS, J. LESAUTER, D. WELSH, S. KAY, D. FOLEY, AND R. SILVER, Exploring spatiotemporal organization of scn circuits, in Proceedings of the Cold Spring Harbor Symposia on Quantitative Biology, Vol. 72, Cold Spring Harbor Laboratory Press, New York, 2007, pp. 527–541, https://doi.org/10.1101/sqb.2007.72.037.
- [55] B.-J. ZANDT, S. VISSER, M. VAN PUTTEN, AND B. TEN HAKEN, A neural mass model based on single cell dynamics to model pathophysiology, J. Comput. Neurosci., 37 (2014), pp. 549–568, https://doi.org/10.1007/s10827-014-0517-5.